AGU PUBLICATIONS

JGR

Journal of Geophysical Research: Atmospheres

RESEARCH ARTICLE
10.1002/2015JD023695

Key Points:
- Noah model physics are augmented to reliably simulate runoff in the source region of Yellow River
- Improved characterization of vertical processes leads to better catchment-scale simulation
- Impeding effect of frozen ground is limited for runoff produce in the source region of Yellow River

Correspondence to:
D. Zheng,
d.zheng@utwente.nl

Citation:
Zheng, D., R. Van der Velde, Z. Su, J. Wen, X. Wang, M. J. Booij, A. Y. Hoekstra, S. Lv, Y. Zhang, and M. B. Ek (2016), Impacts of Noah model physics on catchment-scale runoff simulations, *J. Geophys. Res. Atmos.*, *121*, 807–832, doi:10.1002/2015JD023695.

Received 20 MAY 2015
Accepted 1 JAN 2016

Impacts of Noah model physics on catchment-scale runoff simulations

Donghai Zheng[1,2], Rogier Van der Velde[1], Zhongbo Su[1], Jun Wen[3], Xin Wang[3], Martijn J. Booij[2], Arjen Y. Hoekstra[2], Shihua Lv[3], Yu Zhang[3], and Michael B. Ek[4]

[1]Faculty of Geo-Information Science and Earth Observation, University of Twente, Enschede, Netherlands, [2]Faculty of Engineering Technology, University of Twente, Enschede, Netherlands, [3]Key Laboratory of Land Surface Process and Climate Change in Cold and Arid Regions, Cold and Arid Regions Environmental and Engineering Research Institute, Chinese Academy of Sciences, Lanzhou, China, [4]Environmental Modeling Center of National Centers for Environmental Prediction, Camp Springs, Maryland, USA

Abstract Noah model physics options validated for the source region of the Yellow River (SRYR) are applied to investigate their ability in reproducing runoff at the catchment scale. Three sets of augmentations are implemented affecting descriptions of (i) turbulent and soil heat transport (Noah-H), (ii) soil water flow (Noah-W), and (iii) frozen ground processes (Noah-F). Five numerical experiments are designed with the three augmented versions, a control run with default model physics and a run with all augmentations (Noah-A). Each experiment is set up with vegetation and soil parameters from Weather Research and Forecasting data set, soil organic matter content from China Soil Database, 0.1° atmospheric forcing data from Institute of Tibetan Plateau Research (Chinese Academy of Sciences), and initial equilibrium model states achieved using a single-year recurrent spin-up. In situ heat flux, soil temperature (T_s), and soil moisture (θ) profile measurements are available for point-scale assessment, whereas monthly streamflow is utilized for the catchment-scale evaluation. The comparison with point measurements shows that the augmentations invoked with Noah-H resolve issues with the heat flux and T_s simulation and Noah-W mitigates deficiencies in the θ simulation, while Noah-A yields improvements for both simulated surface energy and water budgets. In contrast, Noah-F has a minor effect. Also, at catchment scale, the best model performance is found for Noah-A leading to a base flow-dominated runoff regime, whereby the surface runoff contribution remains significant. This study highlights the need for a complete description of vertical heat and water exchanges to correctly simulate the runoff in the seasonally frozen and high-altitude SRYR at the catchment scale.

1. Introduction

The Asian water towers, fed from the Himalayas and adjacent Tibetan Plateau, are threatened by a projected decline in the water availability as a result of climate change [*Immerzeel et al.*, 2010]. At the same time, striking ground warming and permafrost degradation are reported [*Guo and Wang*, 2013; *Salama et al.*, 2012; *Wu and Zhang*, 2010; *Wu et al.*, 2013] that will also affect the regional water cycle and ecosystems [*Cheng and Wu*, 2007; *Jin et al.*, 2009; *Wang et al.*, 2012]. The dependence by several billion people on the freshwater supply from the Great Asian Rivers, e.g., Ganges, Brahmaputra, Mekong, Yangtze, and Yellow River, underlines the importance of preserving the high-altitude Asian ecosystem on the Tibetan Plateau. A thorough understanding of the water and heat exchanges at the Tibetan land-atmosphere interface is therefore needed to account for the various feedback on the regional hydrology and available water resources within various climate change scenarios.

Many previous studies [e.g., *Gao et al.*, 2012; *Immerzeel et al.*, 2010; *Lutz et al.*, 2014] have used hydrological models for quantifying the water fluxes and predicting the water availability across the Tibetan Plateau. A substantial part of the Tibetan Plateau is, however, underlain with permafrost and/or subject to seasonally frozen ground, which makes the freeze-thaw process as one of the key components for understanding the surface hydrology of the region. The presence of ice dramatically changes the soil hydraulic and thermal properties [*Farouki*, 1986; *Zhang et al.*, 2008, 2010] that in turn affect the water and heat fluxes [*Gouttevin et al.*, 2012; *Li et al.*, 2010; *Viterbo et al.*, 1999]. While hydrological models constrain the hydraulic conductivity of frozen ground, the implication of phase transition on the energy budget is typically neglected. Likewise, various warm season “soil” and “aboveground” heat transfer processes are not included in the structure of hydrological models. Such incomplete treatment of both cold and warm season energy processes forms a source of uncertainty [*Luo et al.*, 2003] that may be particularly important for high-altitude regions, such as the Tibetan Plateau.

The land surface modeling community, on the other hand, has made significant progress in developing model physics for the effects of the freeze-thaw process on water and energy budgets [*Cherkauer and Lettenmaier*, 1999; *Dankers et al.*, 2011; *Ek et al.*, 2003; *Niu and Yang*, 2006], leading to increased interests for using land surface models (LSMs) for runoff or streamflow modeling across domains with frozen ground [*Finney et al.*, 2012; *Livneh et al.*, 2011; *Slater et al.*, 2007; *Y. Zhang et al.*, 2013]. For instance, *L. Zhang et al.* [2013] and *Xue et al.* [2013] have recently applied LSMs for modeling the runoff regime of the Tibetan Plateau; however, key findings on understanding the land surface process over the Tibetan Plateau [e.g., *Chen et al.*, 2011; *K. Yang et al.*, 2009; *Yang et al.*, 2005; *Zheng et al.*, 2014] have not been thoroughly investigated.

The understanding of the hydrometeorological processes on the Tibetan Plateau has greatly advanced due to the development of data sets collected as part of the various field campaigns and monitoring networks since 1998 [e.g., *Koike*, 2004; *Koike et al.*, 1999; *Ma et al.*, 2008; *Su et al.*, 2011; *Yang et al.*, 2013]. Among the key findings are (i) the diurnally varying roughness length for heat transfer (z_{0h}) is an imperative for reliable surface temperature and turbulent heat simulation [*Chen et al.*, 2011; *Zeng et al.*, 2012; *Zheng et al.*, 2014] and (ii) vertical soil heterogeneity caused by organic matter and root systems are necessary for accurate soil water and heat flow calculations [*Chen et al.*, 2013; *Yang et al.*, 2005]. The above results have been recently incorporated in the Noah LSM and demonstrated that the augmentations improve the simulation of the vertical processes through comparisons with measurements performed at a hydrometeorological station on the Tibetan Plateau [*Zheng et al.*, 2015a, 2015b].

In this study, we investigate the impact of the improved representation of the vertical processes within the Noah LSM on the runoff regime produced at the catchment scale. For this investigation, the source region of the Yellow River (SRYR) in the northeastern part of the Tibetan Plateau and the study period 2001–2010 are selected. Apart from the default Noah LSM, four additional model runs are performed with augmentations to the (i) soil and turbulent heat transport, (ii) soil water flow, and (iii) frozen soil processes, separately as well as combined. The high-resolution (0.1°) data set by *Chen et al.* [2011] developed specifically for China is utilized as atmospheric forcing. Performance of the Noah simulations is assessed at point-scale using in situ soil moisture and temperature measurements and for the model domain using Yellow River discharge measurements. In addition, the spatial distributions of the runoff production mechanisms are quantified across the SRYR for each set of model physics.

This paper is outlined as follows: section 2 introduces the Noah model physics and the augmentations. Section 3 describes the study area and in situ measurements. Section 4 provides a description of the experimental design and data sets utilized for the model setup. Sections 5 and 6 present, respectively, the point-scale and catchment-scale assessment of the model performance in simulating soil states (i.e., moisture and temperature) and discharge. Section 7 provides a discussion on the sensitivity of the simulated runoff production to the combination of model physics, and the impeding effect of frozen ground, as well as the vegetation and soil data sets. Further, section 8 concludes with a summary of the findings in this study.

2. Noah Model Physics

The Noah LSM [*Ek et al.*, 2003] is widely used by the weather and climate modeling community (e.g., the Weather Research and Forecasting (WRF) model community) to quantify the exchange of water and heat at the land-atmosphere interface and is one of the LSMs deployed for NASA's Land Data Assimilation Systems [*Mitchell et al.*, 2004; *Rodell et al.*, 2004; *Xia et al.*, 2012]. The soil-snow-vegetation system is represented as a single heat/water vapor source in Noah for the computation of surface energy and water budgets. A diurnal Penman approach [*Mahrt and Ek*, 1984] linked to a modestly complex canopy resistance scheme [*Chen et al.*, 1996] is utilized for simulating the evapotranspiration, and a simple water balance approach [*Schaake et al.*, 1996] is adopted to simulate the surface runoff. A 2 m homogeneous soil column with four layers of 0.1, 0.3, 0.6, and 1.0 m with increasing thickness toward the bottom is implemented with the diffusivity form of Richards' equation for simulating water flow and the thermal diffusion equation for simulating heat transport [*Mahrt and Pan*, 1984; *Pan and Mahrt*, 1987], with gravitational free drainage from the model bottom assumed. Hydraulic and thermal effects of the freeze-thaw process are considered as described in *Koren et al.* [1999].

The model physics of Noah associated with soil heat transport, soil water flow, and runoff production are described in Appendix A. Readers are referred to existing literature [e.g., *Ek et al.*, 2003; *Niu et al.*, 2011; *van der Velde et al.*, 2009] for additional information. Below we describe the augmentations to the Noah model physics selected for this investigation.

2.1. Noah-H

Overestimation of the turbulent heat fluxes and underestimation of surface and soil temperatures by Noah have been widely reported [*Chen et al.*, 2011; *Niu et al.*, 2011; *Rosero et al.*, 2010; *van der Velde et al.*, 2009; *Zeng et al.*, 2012; *Zheng et al.*, 2014]. Four augmentations have been proposed by *Zheng et al.* [2015b] to mitigate these deficiencies, hereafter referred to as Noah-H.

First, the muting effect of vegetation, modeled as an exponential decay as a function of the green vegetation fraction (GVF) and an empirical muting factor ($\beta_{\text{veg}} = 2.0$), on the soil heat conductivity defining the heat transport from the first layer toward the second layer ($\kappa_{h,1}$) is removed. Second, the exponential decay factor (β_{veg}) imposed on the surface heat conductivity defining the heat transport from the surface to the first soil layer ($\kappa_{h,0}$) is calculated using the ratio of the leaf area index (LAI) over the GVF (i.e., $\beta_{\text{veg}} = 0.5$ LAI/GVF) for unstable atmospheric conditions. Third, Zilitinkevich's empirical coefficient ($C_{\text{zil}} = 0.1$) for the turbulent heat transport is computed as a function of the roughness length for momentum transport ($C_{\text{zil}} = 10^{-0.4z0m/0.07}$) given in *Chen and Zhang* [2009] and *Zheng et al.* [2014]. Fourthly, the impact of organic matter is considered in the parameterization of the thermal heat capacity according to the method proposed by *de Vries* [1963], and the parameterization of the thermal heat conductivity [*Johansen*, 1975; *Peters-Lidard et al.*, 1998] is modified to incorporate the organic matter effect on dry thermal heat conductivity via bulk density and saturated heat conductivity via the geometric mean of the heat conductivities of the materials present within the soil matrix including organic matter.

2.2. Noah-W

Recently, *Chen et al.* [2013], *Su et al.* [2013], and *Xue et al.* [2013] have reported on the inability of the state-of-the-art LSMs to reproduce the soil moisture profiles measured across the Tibetan Plateau. This is attributed to the absence of vertical soil heterogeneity within the model structure that is present within Tibetan ecosystems due to the abundance of plant roots and organic matter in the topsoil. *Zheng et al.* [2015a] have proposed four augmentations to include this vertical soil heterogeneity into the Noah LSM, hereafter referred to as Noah-W.

First, the effect of organic matter on the soil hydraulic properties is considered via the additivity hypothesis, which estimates the hydraulic parameters as a weighted combination of the mineral and organic fractions [*Lawrence and Slater*, 2008; *Zeiliguer et al.*, 2000]. Second, a function is implemented that decays the saturated hydraulic conductivity (K_s) exponentially with soil depth [*Beven*, 1982], whereby the K_s at the reference depth (e.g., surface) is estimated by the Kozeny-Carman equation using the porosity and slope of the water retention curve [*Ahuja et al.*, 1984; *Saxton and Rawls*, 2006]. Third, the vertically uniform root distribution is replaced with an asymptotic function [*Jackson et al.*, 1996; *Y. Yang et al.*, 2009] to better represent the abundance of roots in the topsoil of Tibetan ecosystems. Fourth, the diffusivity form of Richards' equation (equation (A2)) is revised to allow soil water flow simulation across layers with different hydraulic properties [*Hills et al.*, 1989].

2.3. Noah-F

Niu et al. [2011] have recently pointed out that the Noah-simulated impediment of frozen ground for infiltration is too strong, which causes too much surface runoff. Similarly, *Slater et al.* [2007] have concluded that LSMs need to allow more infiltration under frozen ground conditions to adequately simulate the hydrographs of Arctic rivers. Noah approximates by default the fraction of impermeable ground under frozen conditions as a gamma distribution function applied to the total ice content present within the entire 2 m soil column (equations (A7)–(A9)) [*Koren et al.*, 1999]. However, it should be noted that the data sets employed for the development of this approach originate from several Russian river basins and only extend to depths of 0.8 m (see Figure 4 in *Koren et al.* [1999]). Other LSMs [e.g., *Balsamo et al.*, 2009; *Cherkauer and Lettenmaier*, 1999] also utilize the soil ice and water contents of the first 0.5–0.6 m to estimate the fraction of impermeable area (f_{imp}). Moreover, *Wang et al.* [2009] have shown that the critical depth over which the active soil thawing affects surface runoff is around 0.6 m for a Tibetan permafrost watershed. Therefore, we argue that it is more

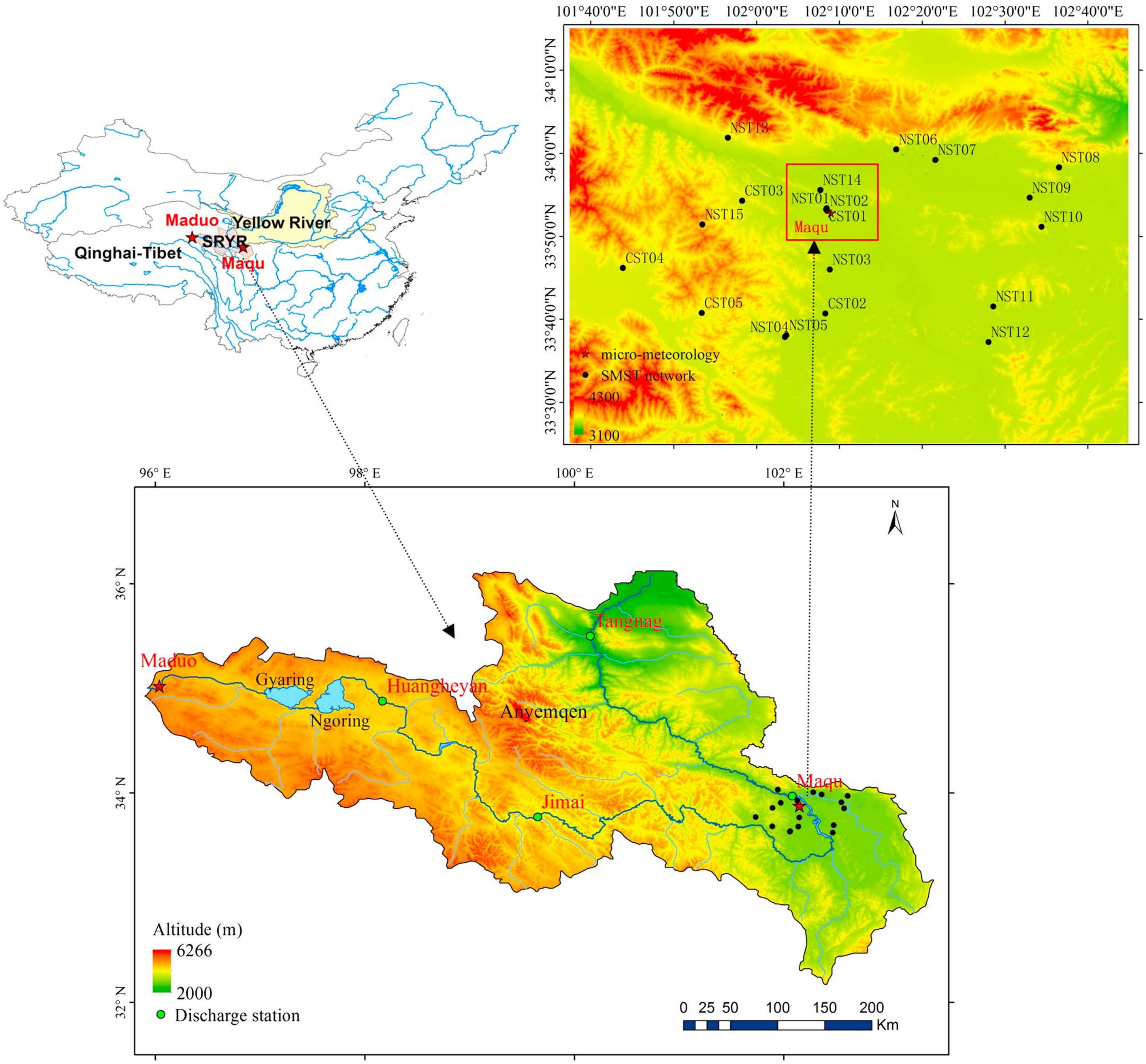

Figure 1. Location of the source region of the Yellow River (SRYR) as well as the Maqu and Maduo stations shown on top of the Shuttle Radar Topography Mission-90 digital elevation model.

appropriate to use a shallower layer thickness within Noah for determining f_{imp}. Since the upper two layers represent only a 0.4 m soil depth, we choose to take the upper three layers, extending up to 1.0 m, as the active thawing region.

In addition, the parameterization proposed by *Niu and Yang* [2006] is adopted for calculating the soil hydraulic conductivity (*K*) and soil water diffusivity (*D*). This formulation computes the transport coefficients as function of the total soil water content reduced by impermeable fraction of each layer, as follows:

$$K = (1 - f_{\mathrm{frz}})K_s(\theta/\theta_s)^{2b+3} \tag{1}$$

$$D = (1 - f_{\mathrm{frz}})D_s(\theta/\theta_s)^{b+2} \tag{2}$$

$$f_{\mathrm{frz}} = \exp[-a(1 - \theta_{\mathrm{ice}}/\theta_s)] - \exp(-a) \tag{3}$$

where K is the hydraulic conductivity (m s^{-1}), D is the soil water diffusivity (m^2 s^{-1}), θ is the total soil water content (m^3 m^{-3}), θ_{ice} is the soil ice content (m^3 m^{-3}), b is an empirical parameter (−) related to the pore size distribution, f_{frz} is the impermeable fraction, a is an adjustable scale-dependent parameter taken as 4.0 as suggested by *Niu et al.* [2011], and the subscript "*s*" stands for the respective quantity under saturated soil conditions. *Niu et al.* [2011] have recommended the above parameterization (equations (1)–(3)) over the default (equations (A3)–(A5)) to allow more transport of water when ice is present in the soil column.

3. Study Area and In Situ Measurements

3.1. Source Region of the Yellow River

The source region of the Yellow River (SRYR; Figure 1) is located in a transition zone from seasonally frozen ground to discontinuous and continuous permafrost in the northeastern part of the Tibetan Plateau [*Jin et al.*, 2009]. The discharge measured at the catchment outlet, Tangnag station, is produced in an area of around 122,000 km^2 that comprises 16.2% of the Yellow River basin in size, while it contributes to more than 35% of the total streamflow [*Zhou and Huang*, 2012]. Hence, the SRYR is widely regarded as the "water tower" of the Yellow River, but it has been a disturbing decline in the streamflow experienced in the past decades [*Hu et al.*, 2011; *Zheng et al.*, 2007; *Zhou and Huang*, 2012].

The elevation in the SRYR varies from 2000 m in the east up to 6300 m in the west with several steeples around the Anyemqen Mountains in the central part of the region. Cold dry winters and rainy summers are characteristics for its climate with annual average daily temperatures ranging from −4 °C to 2 °C decreasing from east to west. The temperature generally remains below 0 °C during the cold season from October to April. The mean annual precipitation varies from 800 mm in the southeast to 200 mm in the northwest, with 75%–90% falling during the monsoon season from June to September [*Hu et al.*, 2011; *Zheng et al.*, 2007]. Alpine grassland and loamy soils dominate the land cover in the region.

Four discharge stations are operated by the Yellow River Conservancy Commission at Huangheyan, Jimai, Maqu, and Tangnag. For this study, only the monthly streamflow data from the Tangnag station are available for the period of 2002–2009, and these are utilized to investigate the performance of Noah in simulating runoff. Streamflow dynamics at Tangnag station are mainly attributed to the climate variability and are not affected by large dams, irrigation diversions, or any other major anthropogenic influences [*Cuo et al.*, 2013].

3.2. Maqu Observation Station

Maqu Climatic and Environmental Observation station (Figure 1) is located in the southeastern part of the SRYR, which is equipped with a micrometeorological observing system and a regional-scale soil moisture and soil temperature (SMST) monitoring network. The micrometeorological observing system consists of a 20 m planetary boundary layer (PBL) tower providing wind speed and direction, air humidity, and temperature measurements at five levels (i.e., 18.15, 10.13, 7.17, 4.2, and 2.35 m) and an eddy covariance system installed at a height of 3.2 m for measuring the turbulent sensible and latent heat fluxes. Instrumentation for measuring the four radiation components (i.e., upward and downward shortwave and longwave radiations), air pressure, and precipitation is also mounted on the PBL tower. The network of 20 SMST monitoring sites covering an area of 40 × 80 km centered on the micrometeorological observing system has been set up primarily for the calibration/validation of satellite-based soil moisture products [*Dente et al.*, 2012; *Su et al.*, 2011].

The data from both the micrometeorological observing system and SMST network are available from November 2009 to December 2010, except that the precipitation data only cover the period of June–September 2010. Because of this, the daily precipitation measurements from the China Meteorological Administration (CMA) station located in the Maqu City, 10 km from the station, are utilized. Four SMST sites (CST01 and NST01/02/14; see Figure 1) of the regional-scale network located in the vicinity of the micrometeorological station (radius < 5 km) are used for validation of the Noah simulations. Additional information on the measurements can be found in *Dente et al.* [2012] and *Zheng et al.* [2014].

3.3. Maduo Observation Station

Maduo station is located in the most western part of the SRYR close to its source (35.03°N, 96.38°E at an elevation of about 4450 m; Figure 1), in which the land cover consists of a mosaic of alpine meadows and wetlands. A continuous permafrost layer is located 3 m below the surface [*Jin et al.*, 2009].

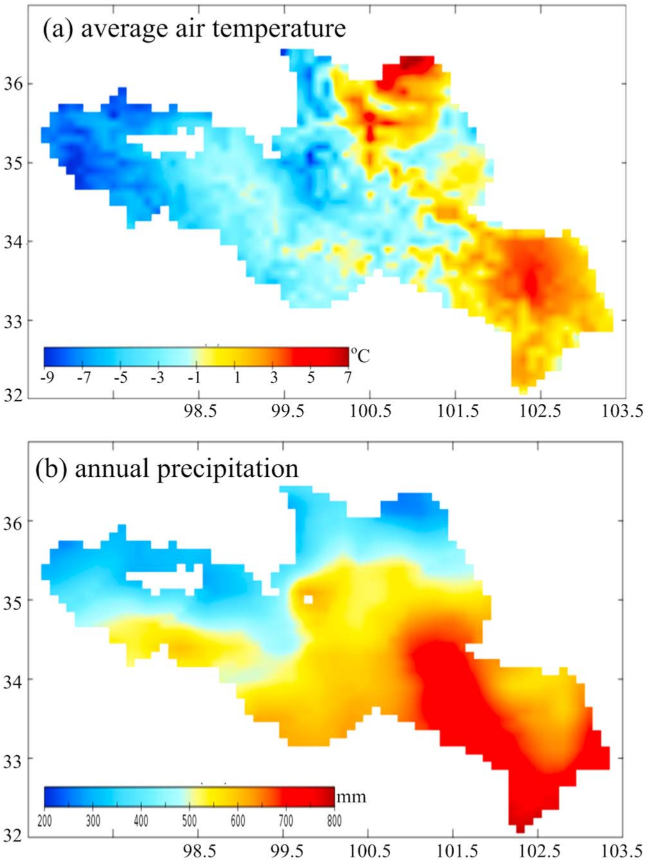

Figure 2. (a) Mean annual 3 hourly air temperature and (b) mean annual precipitation for the SRYR derived from 0.1° ITPCAS atmospheric forcing data covering the period of 2001–2010.

The station includes an automatic weather observation system measuring routinely meteorological variables (i.e., wind speed and direction, air humidity and temperature, and air pressure) at 2.0 m above the surface. Precipitation is measured using a tipping bucket installed at a 1.5 m above the surface. Further, soil moisture and soil temperature at depths of 5, 10, 20, and 40 cm are measured as well.

For this research, the precipitation, soil moisture, and soil temperature profiles measured in the period from November 2009 to December 2010 are utilized for the point-scale assessment (see section 5).

4. Model Implementation

4.1. Atmospheric Forcing

The atmospheric forcing data utilized for the Noah model runs are provided by the hydrometeorological research group of the Institute of Tibetan Plateau Research, Chinese Academy of Sciences (hereafter ITPCAS), which were produced by merging a variety of data sources [*Chen et al.*, 2011], e.g., CMA measurements, Global Land Data Assimilation Systems forcing data set [*Rodell et al.*, 2004], Tropical Rainfall Measuring Mission satellite-observed precipitation [*Huffman et al.*, 2007], and Global Energy and Water Exchanges/Surface Radiation Budget radiation [*Yang et al.*, 2010]. The ITPCAS data set has a spatial resolution of 0.1° and a temporal resolution of 3 h and includes seven forcing variables, i.e., 2 m air temperature (T_a), 10 m wind speed, air pressure, specific humidity, accumulated precipitation (P), and downward shortwave ($S^{\downarrow}$) and longwave ($L^{\downarrow}$) radiations. Additional information on the ITPCAS forcing product and access can be obtained from http://dam.itpcas.ac.cn/rs/?q=data (last verified on 21 December 2015).

The time period under investigation is the episode of 2001–2010, for which Figure 2 shows the spatially distributed mean annual 3 hourly T_a and mean annual P for the SRYR. The maps demonstrate that the spatial T_a distribution is in overall agreement with the topography (Figure 1) with the lowest temperatures in the high-altitude western part of the study area and the highest temperature in regions with the lowest elevation. A similar pattern is noted in the spatial precipitation field with, as expected, the largest rainfall amounts in the humid and lower-altitude southeast. The reliability of the ITPCAS forcing data for the Tibetan Plateau was previously confirmed [*Chen et al.*, 2011; *Guo and Wang*, 2013; *Xue et al.*, 2013] and will be further investigated in section 5 through comparisons to measurements collected at the Maqu and Maduo stations (section 3).

4.2. Vegetation and Soil Parameters

The vegetation and soil parameter data sets used in this study are mainly from the WRF geographic input data set (http://www2.mmm.ucar.edu/wrf/users/download/get_sources_wps_geog.html, last verified on 21 December 2015) and reprocessed using the WRF preprocessing system. Specifically, the 20-category land use data map derived from the Moderate Resolution Imaging Spectroradiometer (MODIS) satellite observations and the hybrid State Soil Geographic Database/Food and Agriculture Organization (FAO) soil texture map are selected for assigning the vegetation and soil types to each grid cell. The green vegetation fraction (GVF) and leaf area index (LAI) are both obtained from the monthly MODIS climatology.

Further, the organic matter content for the updated soil thermal and hydraulic parameterizations (sections 2.1 and 2.2) are taken from the China Soil Database developed by the Land-Atmosphere Interaction Research Group at Beijing Normal University available from http://globalchange.bnu.edu.cn/research/soil2 (last verified on 21 December 2015 [*Shangguan et al.*, 2013]). The organic matter contents available for eight soil layers are linearly interpolated to match with the four layers of the Noah model structure according to *Xia et al.* [2014]. The specification of soil and vegetation parameters for this study is given in Appendix B.

4.3. Experimental Design

Five experiments are designed to assess the impact of the augmentations to the default Noah LSM described in section 2. The Noah LSM is first run with its default model physics described in Appendix A (hereafter Noah). Second, three Noah runs are performed by implementing each set of augmentations described in section 2, respectively. As such, the Noah model is run with augmentations to the model physics of the (i) turbulent and soil heat transport processes (section 2.1, hereafter Noah-H), (ii) soil water flow processes (section 2.2, hereafter Noah-W), and (iii) runoff production under frozen ground conditions (section 2.3, hereafter Noah-F). Lastly, all three sets of augmentations are combined to form the fifth experiment (hereafter Noah-A).

We presently employ Noah LSM version 3.4.1 available from the High-Resolution Land Data Assimilation System (HRLDAS) [*Chen et al.*, 2007]. The codes are modified to make use of the ITPCAS forcing data set (section 4.1) and organic matter content derived from the China Soil Database (section 4.2), as well as to accommodate the augmentations described in section 2. All the experiments are initialized with the same arbitrary hydrologic and thermal states taken constant across the model domain. For instance, the surface and soil temperatures are set to 278.5, 284, 284.5, 282.5, and 280.5 K, respectively, from the surface to the bottom layer, and the soil moisture is initialized as 70% of the porosity. The annual 3 hourly mean T_a from the ITPCAS forcing (Figure 2a) is used as the fixed bottom (8 m) boundary for soil temperature computation.

The model time step is 30 min, and the 3 h ITPCAS forcing is interpolated to the model time step automatically using the HRLDAS functionality. A single-year recurrent spin-up during the period between 1 July 2001 and 30 June 2002 is carried out for each experiment to achieve the equilibrium initial model states, for which 22 model years are needed. The equilibrium is achieved if $|Var^{n+1} - Var^{n}| < 0.001|Var^{n}|$, whereby Var represents each of the model states (e.g., soil moisture/temperature) and n is the spin-up time. The choice of July for the start of the spin-up is based on the suggestions by *Shrestha and Houser* [2010] and *Lim et al.* [2012] that the equilibrium states are more quickly achieved with the spin-up run that started in the summer monsoon months. A single continuous 8.5 year simulation during the period between 1 July 2002 and 31 December 2010 is then conducted for each experiment.

4.4. Experimental Validation

Point (or grid)-scale validation is performed through comparisons of the ITPCAS atmospheric forcing and Noah simulations with the measurements from the Maqu and Maduo stations (section 3) available for the period between November 2009 and December 2010. The ITPCAS forcing (e.g., precipitation and radiation) and Noah simulations (e.g., heat flux, soil moisture, and soil temperature) are extracted from the grid elements where the Maqu and Maduo stations are located. The micrometeorological measurements (e.g., precipitation and radiation and heat flux) from the two stations are directly compared to the corresponding values, while the measured soil moisture and soil temperature profiles within the grid elements are averaged for each measured depth (e.g., 0.05, 0.10, 0.20, 0.40, and 0.80 m) and interpolated to the corresponding midpoint of each model layer (e.g., 0.05, 0.25, and 0.70 m). Specifically, measurements of precipitation, radiation, and latent heat flux (LE), as well as four SMST profiles (i.e., CST01 and NST01/02/14), from the Maqu station are utilized for the analysis. For Maduo station, only precipitation data and one measured soil moisture and temperature profile are available.

Streamflow data from the Tangnag station (section 3.1) integrating spatial information across the entire SRYR are used for the catchment-scale assessment for the period between July 2002 and December 2009. Monthly streamflow (m^3) observations are converted to the area-averaged runoff depth (mm) by dividing by the area of the SRYR (km^2). Surface runoff (R_s) and base flow (or drainage, R_b) simulated by each Noah model run are accumulated over the individual model grid except for the lakes and glaciers in the SRYR and accumulated for each month to produce the monthly area-averaged total runoff by dividing by the number of accumulated model grids. River routing is not applied to the Noah output, since averaging at the monthly scale will largely eliminate the differences between the computed runoff and the time delay implicitly incorporated in instantaneous observed streamflow [*Cai et al.*, 2014; *Pitman et al.*, 1999]. Further, we justify the neglecting of the lake contribution to the total runoff production based on the fact that in the area with two largest lakes in the SRYR, Ngoring (610 km^2) and Gyaring (530 km^2), less than 3.5% of the total SRYR streamflow is produced [*Zheng et al.*, 2007] and direct contribution from the two lakes is even less.

5. Point-Scale Assessment

Figures 3a and 3b show the monthly average of the downward shortwave radiation ($S^{\downarrow}$) and monthly precipitation (P) totals computed from the Maqu measurements (section 3.2) and ITPCAS forcing (section 4.1) for the period between November 2009 and December 2010, and the monthly P totals from the Maduo station (section 3.3) are shown in Figure 4a. The error statistics computed between the measurements and the ITPCAS forcing are shown in these figures as well, i.e., the coefficient of determination (R^2), mean error (ME), and root-mean-square error (RMSE). The agreement noted between the measurements and the ITPCAS forcing supported by the average error statistics, e.g., R^2 of 0.97 and 0.96 and RMSE of 12.77 W m^{-2} and 10.58 mm month^{-1} for $S^{\downarrow}$ and P, respectively, confirms the reliability and suitability of the ITPCAS forcing for this study.

Figures 3c–3g show the monthly average of the measured and simulated latent heat flux (LE), soil temperature (T_s), and liquid soil moisture (θ_{liq}) profiles produced by the five Noah experiments (section 4.3) extracted for the Maqu station, and Figures 4b–4e present the measured and simulated T_s and θ_{liq} profiles for the Maduo station. Tables 1 and 2 list the resulting RMSEs for the Maqu and Maduo stations, respectively. With its default model physics, Noah overestimates the LE (Figure 3c) and underestimates the T_s profile measurements (Figures 3d and 3e or 4b and 4c), and the θ_{liq} profile measurements are consistently underestimated for the entire year (Figures 3f and 3g or 4d and 4e). After implementing the augmentations made to the model physics associated with the turbulent and soil heat transport (section 2.1), the overestimation of LE and underestimation of T_s are greatly ameliorated as can be deduced from the Noah-H results. In comparison to the default Noah model, this reduces the average RMSE computed between the measured and simulated LE and T_s for depths of 5 cm and 25 cm by about 24, 25, and 42%, respectively. Also, an improvement is noted in θ_{liq} simulations as a result of selected augmentations. The reason for this is that Noah-H tends to produce less turbulent heat fluxes leading to warmer and wetter soil profiles [*Zheng et al.*, 2015b].

Notably, the θ_{liq} underestimation by the default Noah model is significantly ameliorated through implementation of the asymptotic vertical root distribution as well as the modified soil hydraulic parameterization with consideration of the organic matter effect (section 2.2) as applied in the Noah-W run. This leads to a reduction in the average RMSE computed between the simulated and measured θ_{liq} by about 49 and 41% for the upper two soil layers. On the other hand, Noah-W augmentations lead to a somewhat degraded model performance with respect to the simulation of LE and T_s. The explanation for this is that wetter soil profiles are favorable for evapotranspiration and thus result in a LE overestimation as noted in Figure 3c, which in turn causes the T_s underestimation seen in Figures 3d and 3e and Figures 4b and 4c. Noah-F produces a slight improvement in the surface soil moisture simulation by allowing a larger liquid water movement into the frozen front during the cold season at the cost of a degraded soil moisture simulation for the lower layer in comparison to the default Noah model.

Noticeable improvements are found in the simulations of LE, T_s, and θ_{liq} by including all the augmentations described in section 2 made to the Noah model physics (i.e., Noah-A model run). In this case the average RMSEs computed between the measurements and simulations reduced by about 15, 28, 43, 64, and 61% for LE, T_{s5}, T_{s25}, $\theta_{\text{liq}5}$, and $\theta_{\text{liq}25}$, respectively, in comparison to the default Noah model run. This improvement in the simulations is somewhat expected since Noah-A produces less turbulent heat fluxes and a warmer soil profile through implementation of the Noah-H augmentations and a wetter soil profile as a result of the Noah-W augmentations. This demonstrates the necessity to include complete and robust descriptions of both surface energy and water budget processes in model physics for reliable simulations of heat and mass exchanges at the land-atmosphere interface of the SRYR.

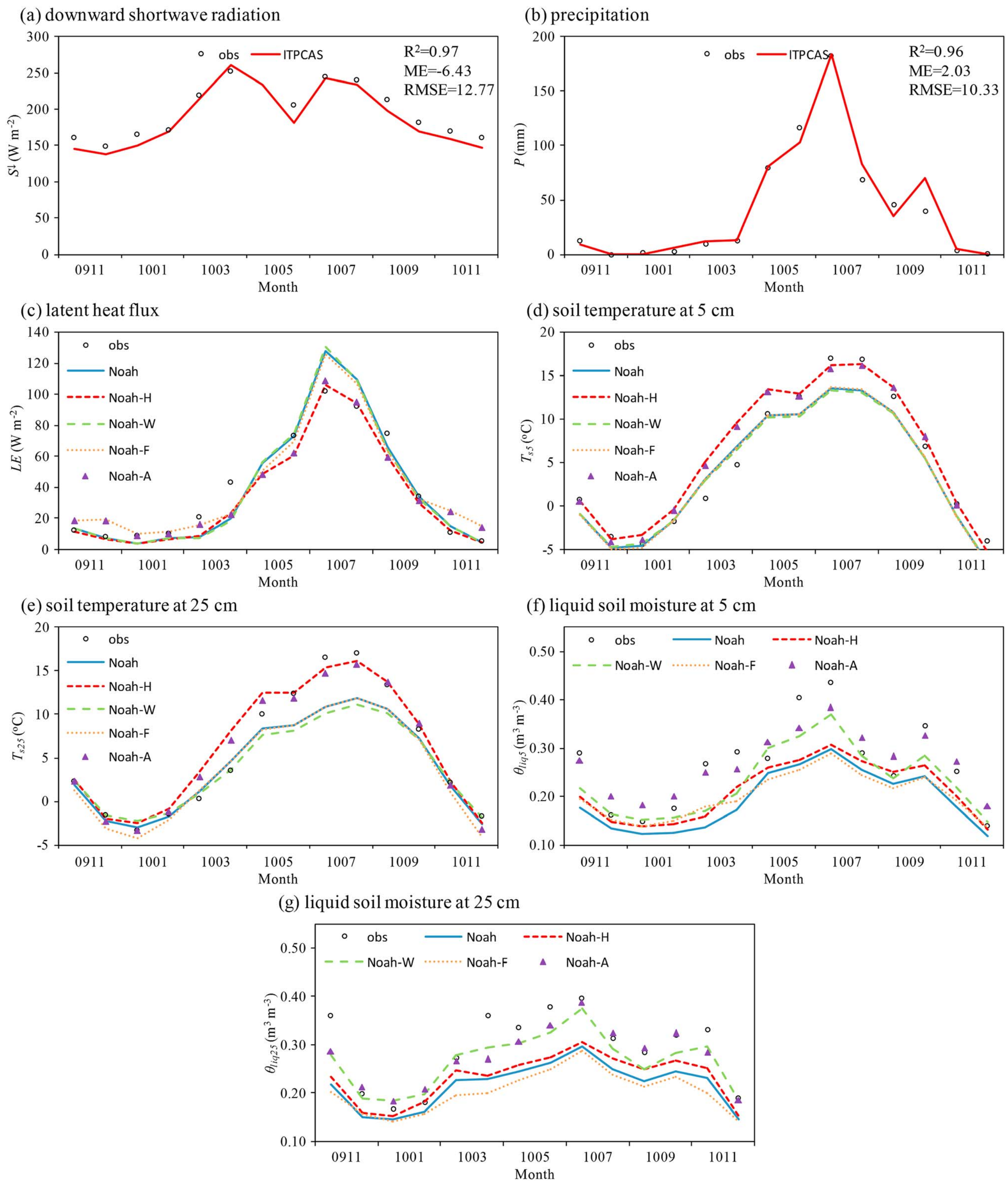

Figure 3. Comparisons of monthly (a) averaged downward shortwave radiation, (b) accumulated precipitation, (c) averaged latent heat flux, averaged soil temperature from depths of (d) 5 cm and (e) 25 cm, and averaged liquid soil moisture from depths of (f) 5 cm and (g) 25 cm measured at the Maqu station with simulations extracted from the ITPCAS forcing and five Noah numerical experiments for the period of November 2009–December 2010.

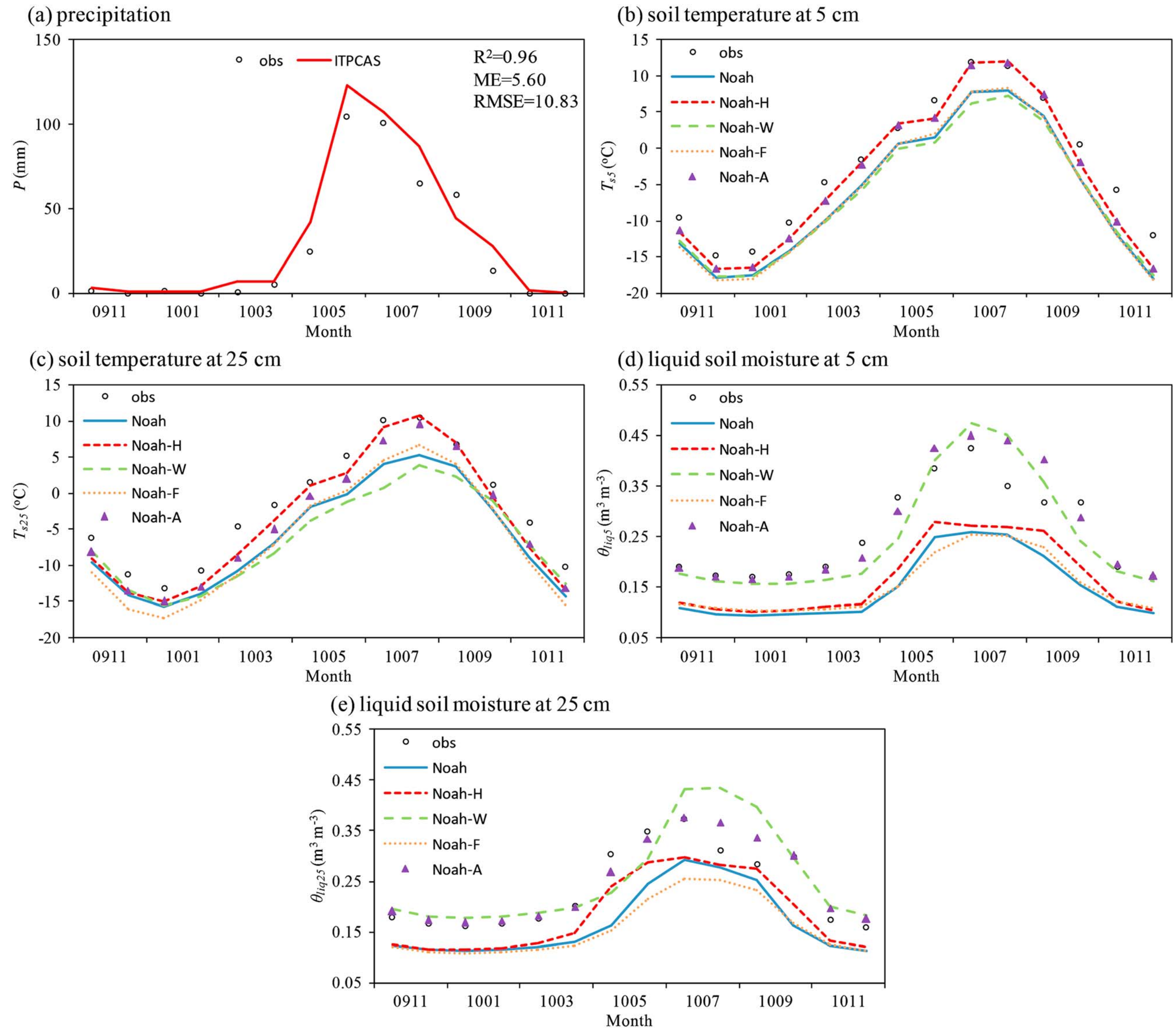

Figure 4. Comparisons of monthly (a) accumulated precipitation, averaged soil temperature from depths of (b) 5 cm and (c) 25 cm, and averaged liquid soil moisture from depths of (d) 5 cm and (e) 25 cm measured at the Maduo station with simulations extracted from the ITPCAS forcing and five Noah numerical experiments for the period of November 2009–December 2010.

Table 1. Root-Mean-Square Error (RMSE) Computed Between the Measurements Collected From the Maqu Station and the Simulated Latent Heat Flux (*LE*), Soil Temperature (T_s), and Liquid Soil Moisture (θ_{liq}) for Depths of 5 cm and 25 cm Produced by Eight Noah Model Runs for the Period of November 2009–December 2010

RMSE	*LE* (W m^{-2})	T_{s5} (°C)	T_{s25} (°C)	θ_{liq5} (m^3 m^{-3})	θ_{liq25} (m^3 m^{-3})
Noah	11.66	2.05	2.56	0.090	0.084
Noah-H	8.82	1.93	1.63	0.074	0.072
Noah-W	12.52	2.10	2.91	0.055	0.039
Noah-F	11.76	2.06	2.69	0.083	0.099
Noah-A	9.97	1.83	1.44	0.036	0.038
EXPS1a	8.85	1.88	1.47	0.038	0.031
EXPS1b	9.54	1.85	1.58	0.066	0.077
EXPS1c	12.52	2.15	3.01	0.050	0.059

Table 2. Root-Mean-Square Error (RMSE) Computed Between the Measurements Collected From the Maduo Station and the Simulated Soil Temperature (T_s) and Liquid Soil Moisture (θ_{liq}) for Depths of 5 cm and 25 cm Produced by Eight Noah Model Runs for the Period of November 2009–December 2010

RMSE	T_{s5} (°C)	T_{s25} (°C)	θ_{liq5} ($m^3\ m^{-3}$)	θ_{liq25} ($m^3\ m^{-3}$)
Noah	4.31	4.35	0.116	0.077
Noah-H	2.42	2.31	0.097	0.055
Noah-W	4.46	5.05	0.048	0.055
Noah-F	4.31	4.70	0.114	0.087
Noah-A	2.41	2.52	0.038	0.025
EXPS1a	2.35	2.57	0.048	0.039
EXPS1b	2.63	2.87	0.095	0.067
EXPS1c	4.50	5.10	0.045	0.051

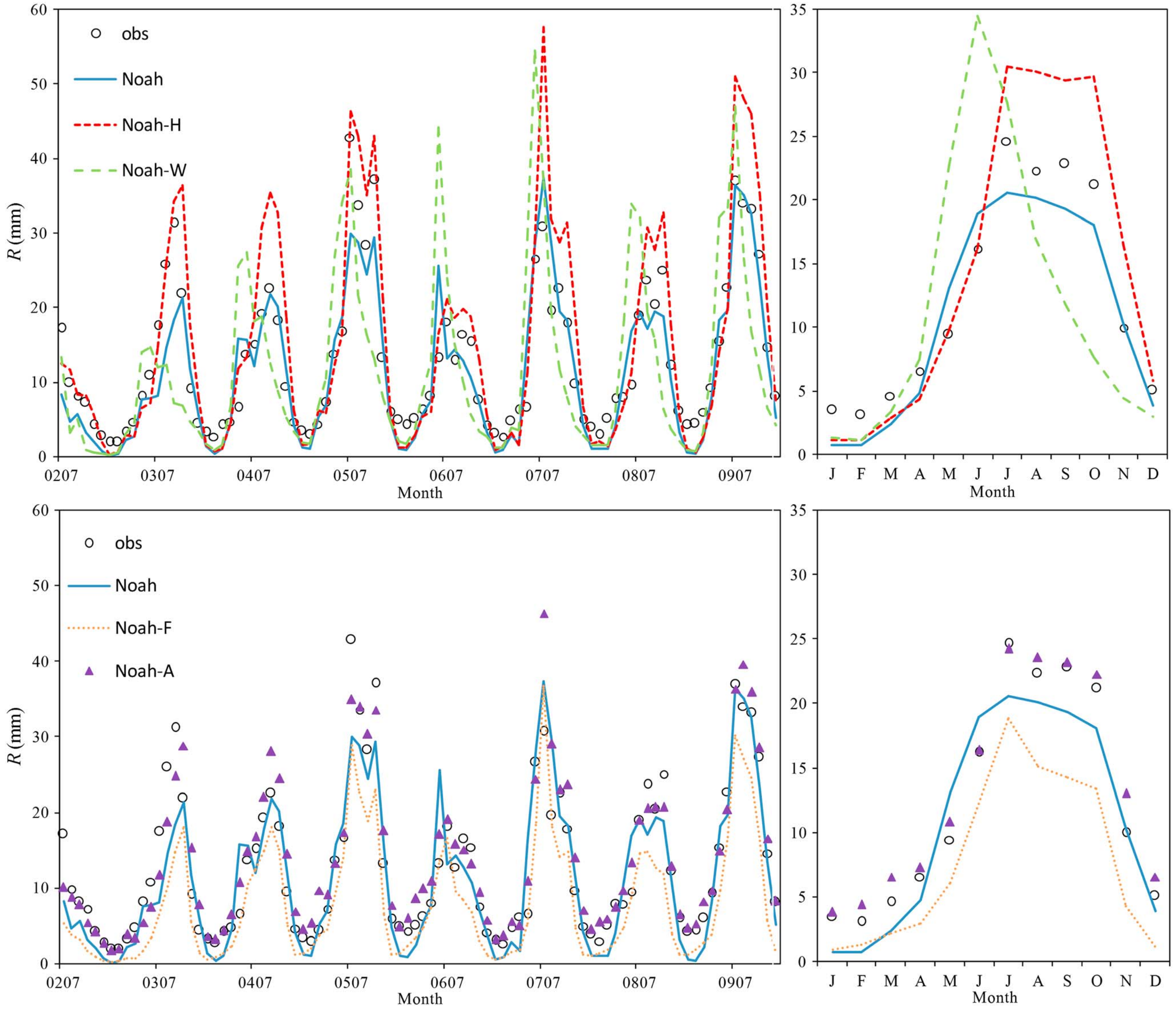

Figure 5. Comparisons of measured and simulated (left) monthly accumulated and (right) multiyear monthly averaged total runoff (*R*) produced using five numerical experiments for the period of July 2002–December 2009.

Table 3. Coefficient of Determination (R^2), Mean Error (ME), Root-Mean-Square Error (RMSE), and Nash-Sutcliffe Efficiency (NSE) Computed Between the Measured and Simulated Total Runoff Produced by All the Numerical Experiments for the Period of July 2002–December 2009

Experiments	R^2	ME (mm)	RMSE (mm)	NSE
Noah	0.825	−1.43	4.44	0.80
Noah-H	0.900	2.59	6.33	0.59
Noah-W	0.381	−0.96	9.88	−0.01
Noah-F	0.868	−4.83	6.11	0.61
Noah-A	0.882	1.08	3.62	0.86
EXPS1a	0.733	2.52	6.47	0.57
EXPS1b	0.885	0.13	3.93	0.84
EXPS1c	0.825	−2.92	5.46	0.69
EXPS2a	0.894	0.92	3.55	0.87
EXPS2b	0.894	0.91	3.54	0.87
EXPS3a	0.886	1.45	3.76	0.85
EXPS3b	0.882	1.11	3.63	0.86
EXPS3c	0.886	1.49	3.77	0.85

6. Catchment-Scale Assessment

6.1. Areal Average

Figure 5 shows the monthly accumulated area-averaged measured and simulated total runoff depth (R) produced by the five Noah experiments (section 4.3) for the period of July 2002–December 2009, whereby the measured, Noah, Noah-H, and Noah-W total runoff are presented in the top plot and the measured, Noah, Noah-F, and Noah-A in the bottom plot. In addition, the monthly R averaged for the 7.5 year period is shown for both measurements and simulations. Table 3 provides the respective error statistics, i.e., R^2, ME, RMSE, and Nash-Sutcliffe efficiency (NSE). Noah, with its default model physics, is able to capture the observed monthly R dynamics reasonably well, which is also supported by R^2 and NSE values larger than 0.80. However, underestimations of the observed R are noted during the summer season from July to October and in the cold season from January to March.

Although Noah-H greatly improves the simulations of the turbulent and soil heat transport (section 5), it largely overestimates the R observed in the period from July to November (>6 mm on the average) and yields poor error statistics in terms of ME, RMSE, and NSE. However, Noah-H produces R that agrees well with the measurements made in the transition season (i.e., May and June) as well as a better estimate of R^2. Likewise the improved soil moisture profile simulation achieved with Noah-W (section 5) does not automatically implicate that its R simulations agree well with the measurements. In fact, the plots, as well as the error statistics, suggest that Noah-W represents the worst performance in simulating R. In particular, the simulated R peaks early, significantly overestimating the measurements between May and July (>10 mm on the average), while significant underestimations of measured R are found for September and October. Also, the performance of Noah-F in simulating the hydrograph is poorer than the default model with year-round underestimations of the monthly measured R.

Only when all augmentations are implemented, viz., Noah-A, is an improved performance in simulating R achieved with respect to the default model. The underestimations of the monthly R across the summer and cold seasons are largely resolved by including the augmentations for heat, soil water, and frozen ground processes. Hence, the error statistics are improved by about 7, 24, 19, and 8% for R^2, ME, RMSE, and NSE, respectively, with respect to the Noah experiment. As such, these results eloquently confirm the findings of section 5 at catchment scale via runoff on the need for including complete descriptions of surface energy and water budget processes in model physics.

Further analysis will be given below to address the reason for such different performances in simulating R between the five Noah experiments as shown previously. In support of the further analysis, Figure 6 presents the monthly averaged total runoff (R), surface runoff (R_s), and base flow (R_b) for each experiment. Additionally, Figure 7 shows the precipitation (P), snowmelt, fraction of impermeable frozen area (f_{imp}), liquid (θ_{liq150}), and total (θ_{150}) soil moisture at the bottom layer (e.g., 150 cm).

First of all, we note that all experiments produce comparable snowmelt as seen in Figure 7a. Noah with its default model physics produces f_{imp} values varying from 0.18 to 0.27 in the first half year (Figure 7b). Precipitation and/or snowmelt simulated for these impermeable frozen areas results in R_s (see equation (A6)). As the ice content, viz., θ_{150} (Figure 7d)-θ_{liq150} (Figure 7c), is substantial in the first half of the year, the drainage or R_b remains low and R_s component dominates the R simulated by Noah (Figure 6a). The impermeable frozen area (f_{imp}) disappears gradually during the warm season (June–October; Figure 7b) as the ice in the soil profile thaws. More water can therefore infiltrate into the soil column increasing θ_{liq150} (Figure 7c) and the drainage from the soil bottom (see equation (A10)), which leads to the simulated R being governed by R_b with peaks in

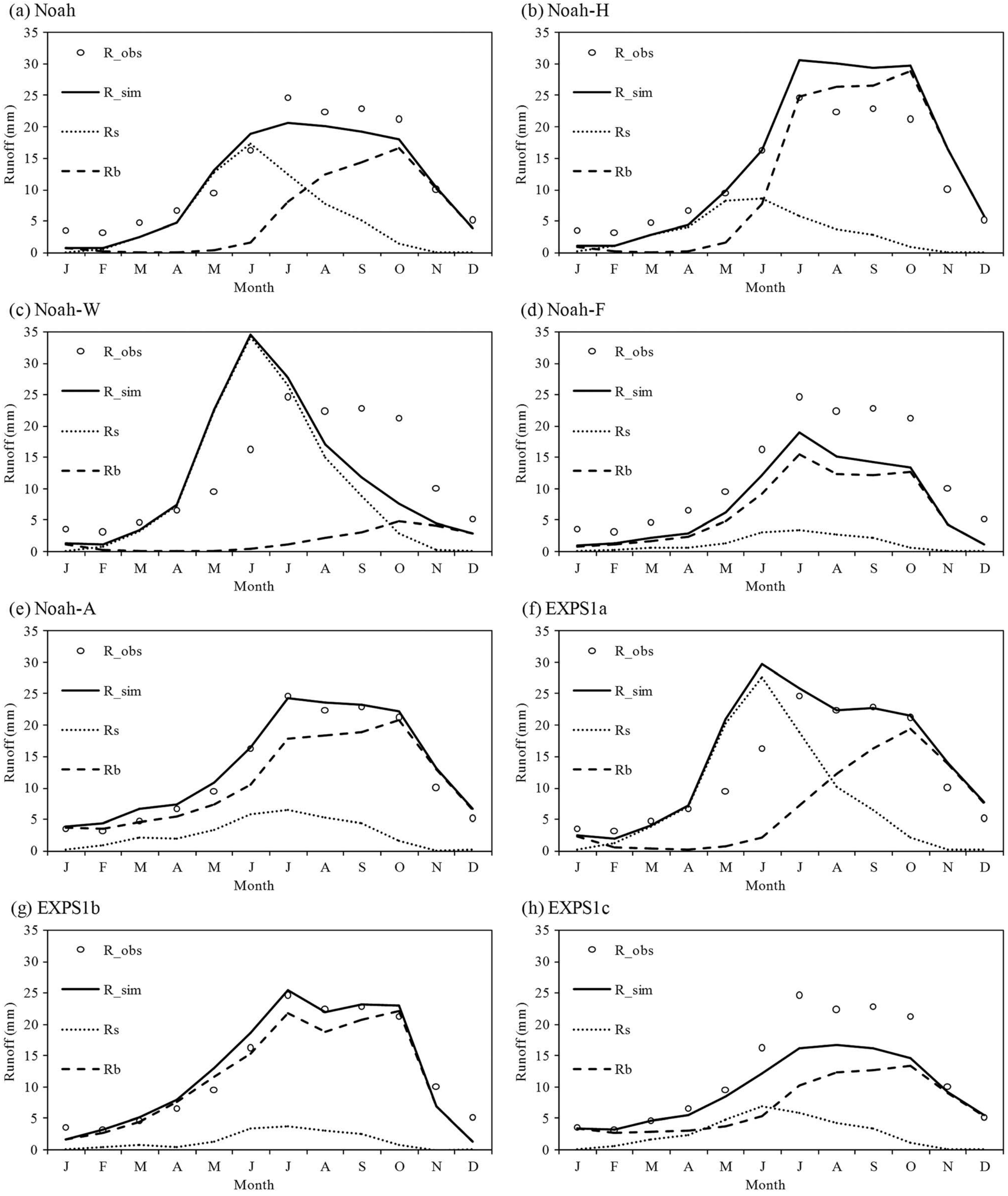

Figure 6. Monthly averaged measured runoff (*R*_obs), simulated total runoff (*R*_sim), surface runoff (R_s), and base flow (R_b) produced using (a) Noah, (b) Noah-H, (c) Noah-W, (d) Noah-F, (e) Noah-A, (f) EXPS1a, (g) EXPS1b, and (h) EXPS1c numerical experiments for the period of July 2002–December 2009.

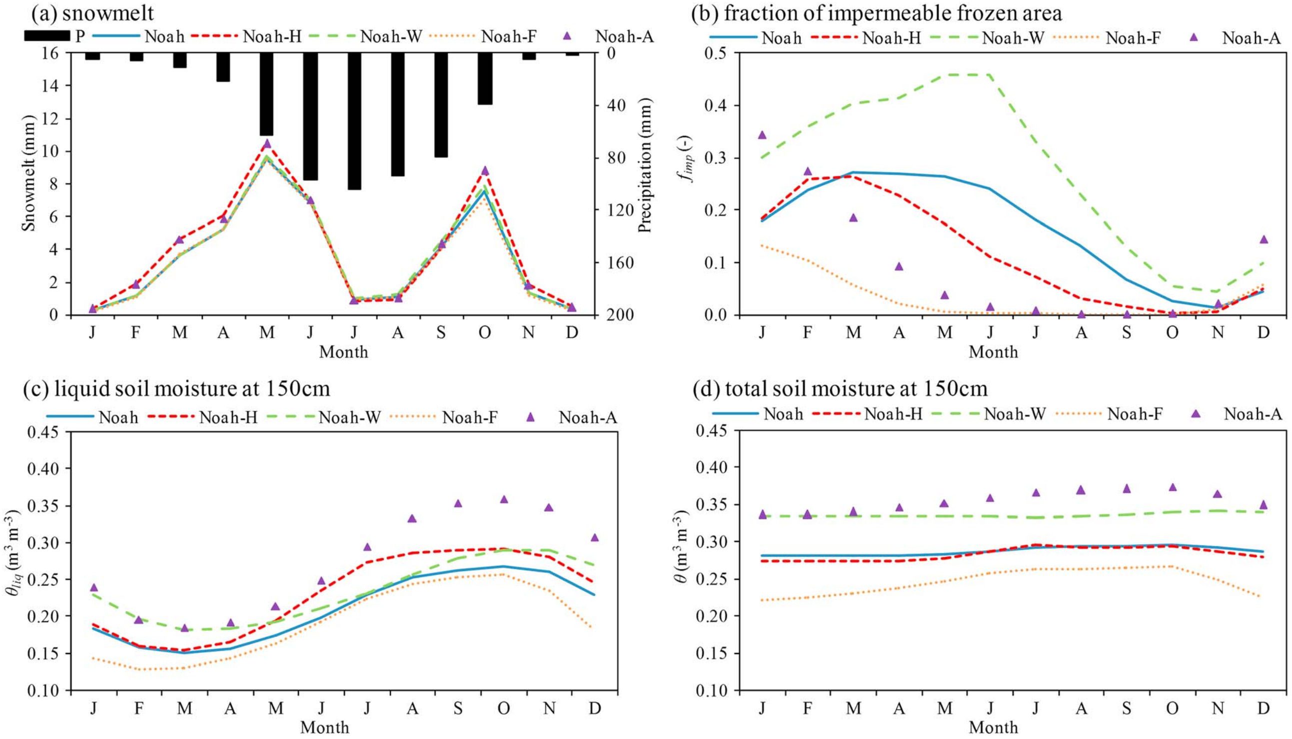

Figure 7. Comparisons of the simulated monthly averaged (a) snowmelt, (b) fraction of impermeable frozen area, (c) liquid, and (d) total soil moisture at depth of 150 cm produced by five numerical experiments for the period of July 2002–December 2009.

October (Figure 6a). At the onset of the cold season, e.g., October–December, the R_b and R decline (Figure 6a) due to the absence of precipitation (Figure 7a) in combination with an increase in the ice content in the bottom soil layer. Notably, the larger θ_{150} (Figure 7d) in comparison to $\theta_{\text{liq}150}$ (Figure 7c) indicates that frozen conditions occur at least in portions of the study domain (i.e., permafrost versus seasonally frozen ground). Since Noah overestimates the evapotranspiration, and produces colder and drier soil profiles in comparison to the measurements (section 5), underestimations of the measured R are noted from July to October (warm season) and from January to March (cold season; Figures 5 and 6a).

Since Noah-H produces generally warmer temperature profiles comparing to the default Noah (section 5), the onset of the thawing of ice within the soil profile is simulated earlier in the year. Therefore, the seasonal f_{imp} decrease (Figure 7b) and $\theta_{\text{liq}150}$ increase (Figure 7c) are already noted starting from March causing a comparable shift in the transition from a R_s- to a R_b-dominated total runoff (Figure 6b). This leads to a good match with the measurements between May and June but to considerable runoff overestimations for the monsoon months, e.g., July, August, and September (Figures 5 and 6b). The larger simulated R_b can be attributed to the assumption of homogeneous soil properties within Noah that leads to overestimation of saturated hydraulic conductivity (K_s) at the bottom soil layer [*Zheng et al.*, 2015a] causing a lower θ_{150} (Figure 7d). Noah-W produces a wetter soil with respect to the default Noah (section 5) and larger ice content across the profile (Figures 7c and 7d), which results in a larger f_{imp} (see equations (A7)–(A9) and Figure 7b) and, thereby, a strongly R_s-dominated total runoff (Figure 6c). This explains the early R peaks and a simulated shape of the hydrograph that does not match well with the measurements (Figures 5 and 6c). In contrast, Noah-F produces the smallest f_{imp} (Figure 7b) leading to more infiltration and a strongly R_b-dominated total runoff (Figure 6d) allowing for a large liquid water movement under frozen ground conditions, consistent with the findings of *Sato et al.* [2008]. Since the Noah-F produces a drier soil for the deep layers in comparison to the default Noah (section 5), less water (Figures 7c and 7d) is available for the runoff production via R_b causing the underestimation of R year-round (Figures 5 and 6d).

Figure 5 and the error statistics in Table 3 already demonstrate that Noah captures the measured hydrograph best when all augmentations are implemented (Noah-A). With the set of model physics included in Noah-A,

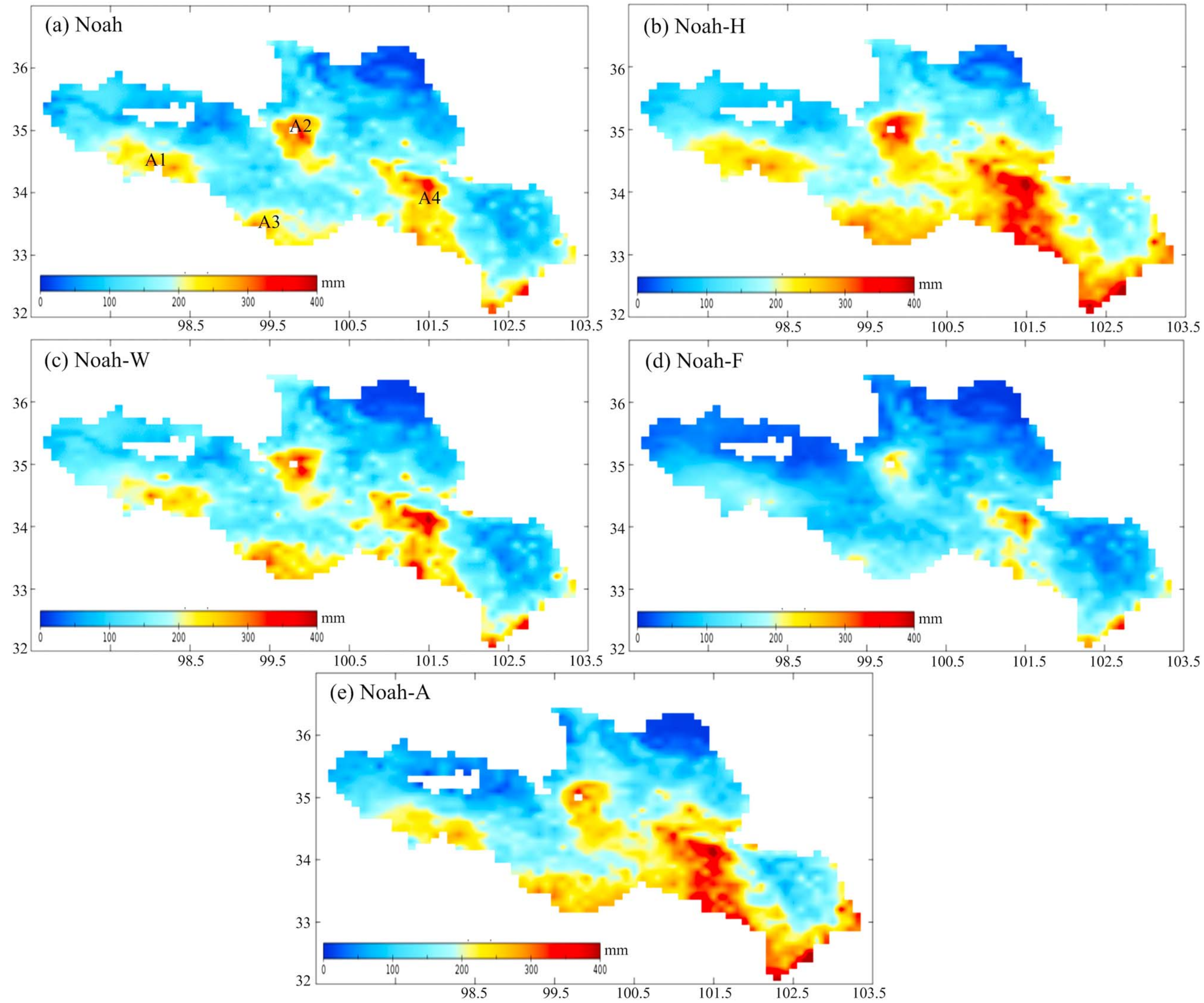

Figure 8. Maps of annual mean total runoff across the SRYR produced by (a) Noah, (b) Noah-H, (c) Noah-W, (d) Noah-F, and (e) Noah-A numerical experiments for the period of July 2002–December 2010.

the ice content is simulated in such manner that f_{imp} can be large in winter ($>$0.3) and decreases sharply at the end of the cold season to approach zero in the warm season (June–October; Figure 7b). As such, Noah-A enables the infiltration into soil column during spring and summer and the retention of soil water year-round by accounting for the effects of organic matter on the soil hydraulic properties that leads to wetter soil profiles (e.g., Figures 7c and 7d). Furthermore, Noah-A is able to release the water from the soil bottom slowly throughout the entire year due to the implementation of the exponential decay function for K_s as well as the new hydraulic parameterization (see equations (1)–(3)), whereby R_b is the main component year-round and thus plays an important role in the simulation of the hydrograph (Figure 6e). This simulated runoff regime is in line with the recommendations of *Slater et al.* [2007] for the simulation of the hydrographs of Artic rivers with LSMs.

6.2. Spatial Variation

Figure 8 shows the spatial distribution of annual mean R over the SRYR produced by the five experiments during the period between July 2002 and December 2010. Four distinct regions of runoff production can be deduced from the R distribution produced by the Noah with default model physics (Figure 8a), e.g., (i) region A1 located at the western high-altitude area (see Figure 1), (ii) region A2 located at the central Anyemqen Mountains, (iii) region A3 located at the southwestern high-altitude area near Jimai discharge station, and (iv) region A4 located near Maqu discharge station in the region with high precipitation (see Figure 2b).

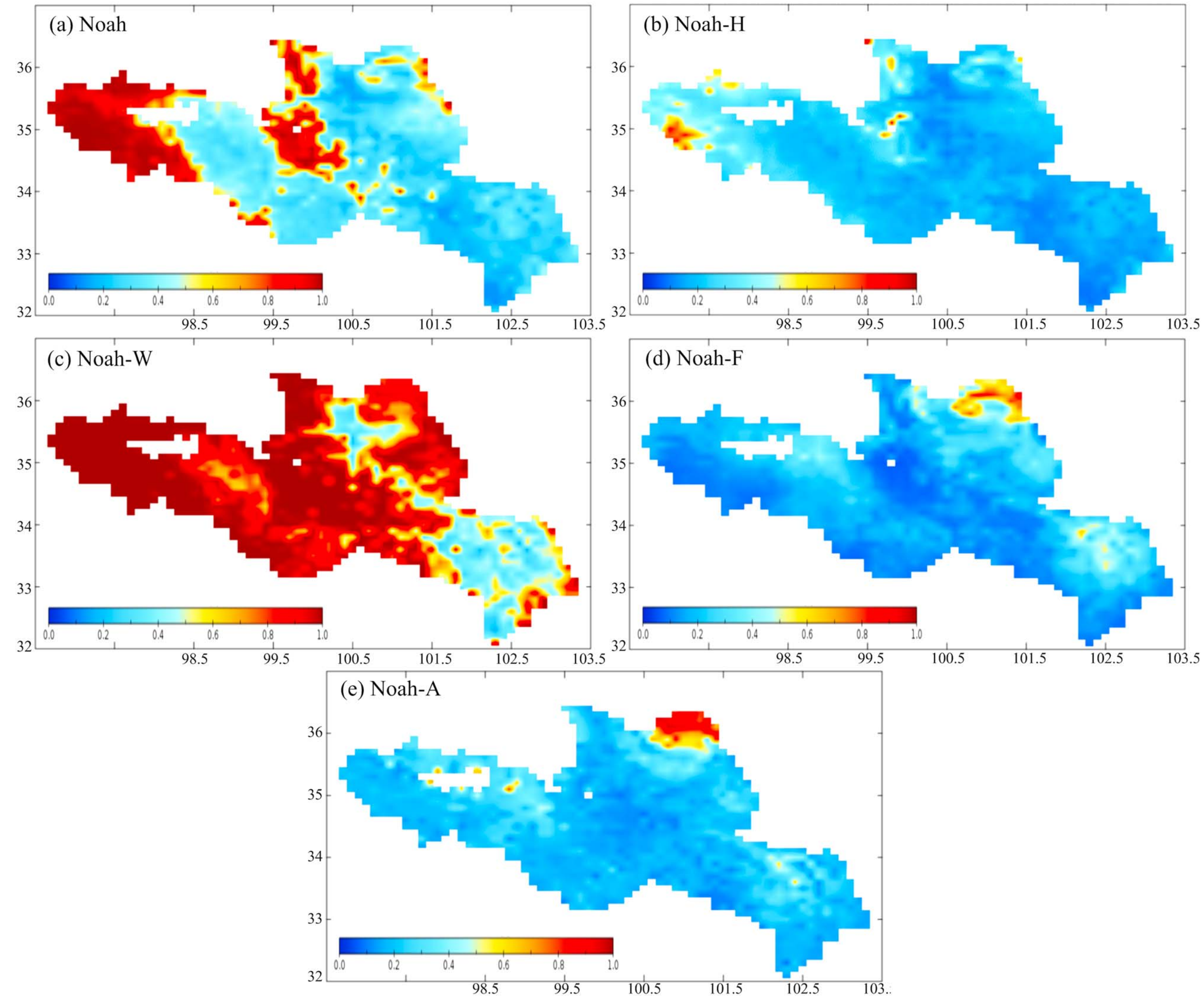

Figure 9. Maps of annual mean surface runoff as fraction of the total runoff for the SRYR produced by (a) Noah, (b) Noah-H, (c) Noah-W, (d) Noah-F, and (e) Noah-A numerical experiments for the period of July 2002–December 2010.

The other experiments produce a similar spatial R distribution as the default Noah model, which in general follows the spatial P distribution. Hence, the high-precipitation regions form the source regions of runoff production, whereby the largest production simulated by each of the five experiments that takes place between Jimai and Maqu discharge stations was previously reported in *Zheng et al.* [2007].

In further analysis, Figure 9 shows the annual mean R_s as a fraction of R produced for the five experiments. In addition, Figure 10 presents the annual averaged f_{imp} for the default Noah and Noah-A models. In the comparison of Figures 8 and 9, it can be deduced that the runoff produced by the Noah with default model physics in regions A1 and A2 mainly consist of the R_s component, while R_b dominates the production in regions A3 and A4 due to a relatively small f_{imp} (Figures 9a and 10a). The overall warmer temperature simulated by Noah-H leads to a smaller f_{imp} (Figure 7b), and more water infiltrates into the soil column, which results in a smaller contribution of R_s across the SRYR (Figure 9b). Since Noah-H simulates less evapotranspiration (*ET*, e.g., Figure 3c) and less soil ice in comparison to the default Noah, more water is available (Figure 7c) for drainage from the bottom of the soil column (or R_b) explaining for the larger runoff volume seen in the extended source regions A1–A4 (Figure 8b). The spatial distribution of Noah-W R production is similar to the default Noah (Figures 8a and 8c) but is characterized by a larger f_{imp} causing R_s to dominate the R production (Figure 9c). Conversely, Noah-F simulates less f_{imp}, and therefore, the R_s contribution is small (Figure 9d), but generates drier soil at the lower layers with respect to the default Noah (section 5) causing less water (Figure 7d) to be available for the runoff production via R_b (Figure 8d).

With implementation of all augmentations, Noah-A produces a similar spatial R distribution as Noah-H (Figures 8b and 8e) but smaller in magnitude. In general, the R_s as a fraction of the total runoff is less than 0.4 (Figure 9e), and therefore, the simulated hydrograph is governed by the R_b as concluded above. Figure 10 illustrates that the difference in f_{imp} simulated by the Noah-A and Noah models is responsible for the respective magnitudes of R_s and R_b as contributions to the total runoff production and overall performance. These results underline the need for a complete description of both cold and warm season hydrometeorological processes for accurately simulating the impeding effect of frozen ground and runoff production.

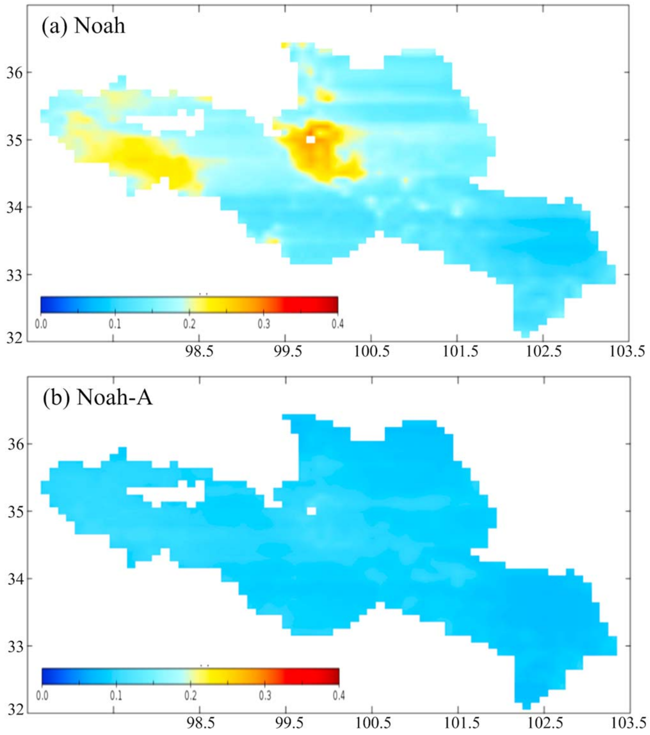

Figure 10. Maps of annual averaged fraction of impermeable frozen area for the SRYR produced using (a) Noah and (b) Noah-A numerical experiments for the period of July 2002–December 2010.

7. Sensitivity Test

7.1. Alternative Combinations of Noah Model Physics

Section 6 demonstrates that Noah captures the measured hydrograph best when all augmentations are implemented (Noah-A) and that the other experiments with each of the individual augmentations (i.e., Noah-H, Noah-W, and Noah-F) perform worse in simulating the runoff with respect to the default Noah model run. Three additional experiments are carried out to further investigate the behavior of the simulated hydrograph when a combination of two augmentations is selected, e.g., Noah-H + Noah-W (hereafter EXPS1a), Noah-H + Noah-F (EXPS1b), and Noah-W + Noah-F (EXPS1c). The other settings are kept the same as described in section 4.3.

The RMSEs for the point-scale assessment of these three experiments are also given in Tables 1 and 2, which show that only EXPS1a performs comparable to Noah-A in reproducing the measured LE and soil moisture and temperature states. This demonstrates that the augmentations invoked with Noah-H and Noah-W are needed to improve the simulation of heat and water budgets at point scale with respect to the default Noah model structure. The error statistics for the catchment-scale assessment are included in Table 3 and suggest that only EXPS1b produces runoff simulations comparable to Noah-A. This highlights that the combination of augmentations invoked with Noah-H and Noah-F forms the key toward improving the runoff simulations.

In support of further analysis, Figure 11 presents the monthly and area-averaged total runoff (R), fraction of impermeable frozen area (f_{imp}), liquid (θ_{liq150}), and total (θ_{150}) soil moisture at the bottom layer resulting from EXPS1a–S1c, whereby separating R into surface runoff (R_s) and base flow (R_b; included in Figure 6). EXPS1a produces a similar f_{imp} evolution as Noah-W (Figures 7b and 11b), but through the implementation of the Noah-H augmentations, a shift is noted in the transition from R_s- to R_b-dominated total runoff and where R_b is much larger (Figures 6c and 6f). The wetter soil profiles produced by EXPS1a (e.g., Figures 11c and 11d) are favorable for the R volume that leads to a better match with the runoff depth observed from July to October in comparison to the default (Figure 11a). EXPS1a, however, overestimates the R in May and June similar to Noah-W due to an exaggerated R_s component caused by the large f_{imp}. The shape of the hydrograph and its

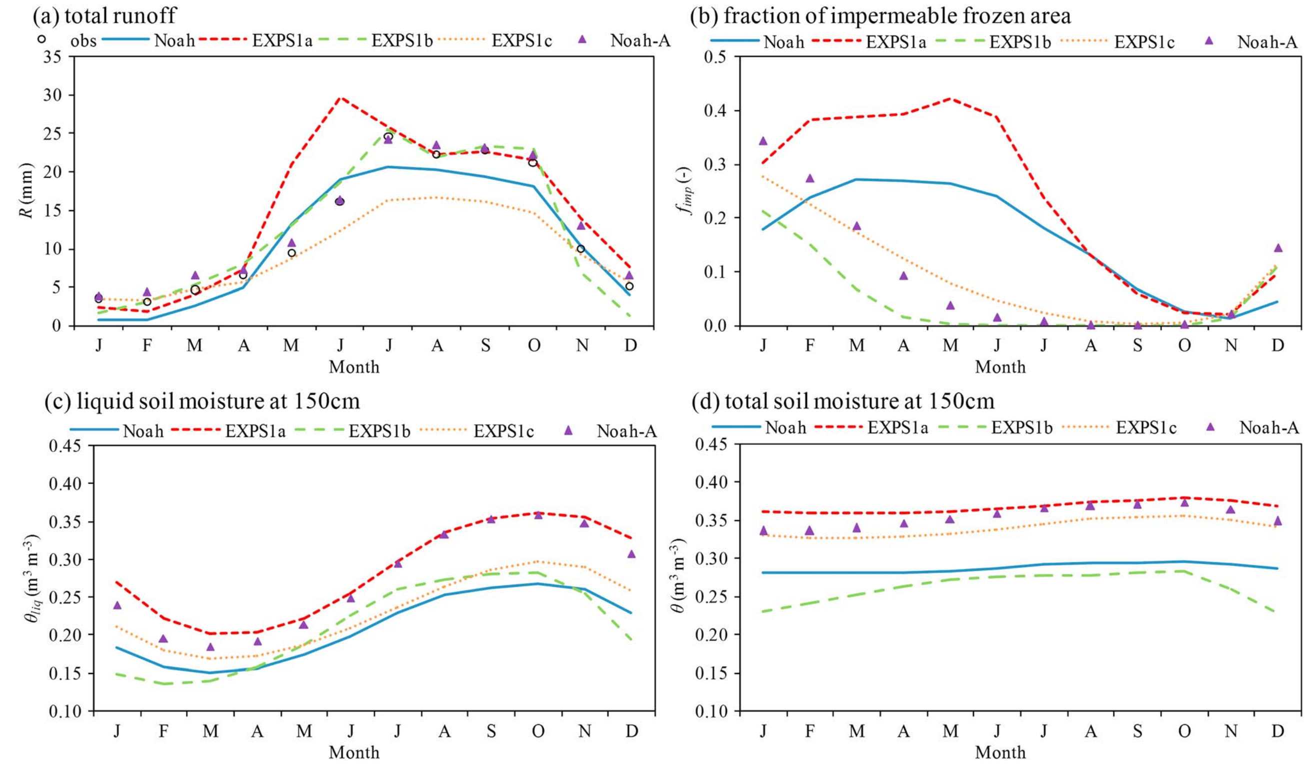

Figure 11. Comparisons of the measured and simulated monthly averaged (a) total runoff, (b) fraction of impermeable frozen area, (c) liquid, and (d) total soil moisture at depth of 150 cm produced by EXPS1a–S1c for the period of July 2002–December 2009.

separation into R_s and R_b components produced by EXPS1b are similar to Noah-F (Figures 6d and 6g). EXPS1b, due to the inclusions of the Noah-H augmentations, simulates higher moisture contents for the bottom soil layer that yields a larger R_b volume, which resolves the underestimation of R seen within the Noah-F results. As such, the total runoff production simulated by EXPS1b is comparable to the results obtained with Noah-A. The f_{imp} (Figure 11b) as well as the R partitioning following from the EXPS1c simulations are comparable to Noah-A (Figures 6e and 6h). However, EXPS1c results in an underestimate of the R measured from June to October (Figure 11a) due to the presence of larger ice contents in the deep layer (Figures 11c and 11d), which is the cause for less R_b. In conclusion, the combination of Noah-H and Noah-W augmentations yields superior soil states (e.g., moisture and temperature) that are needed to reliably simulate the R_b component, whereas the Noah-F augmentations reduce the simulated f_{imp} necessary for a reliable R_s quantification.

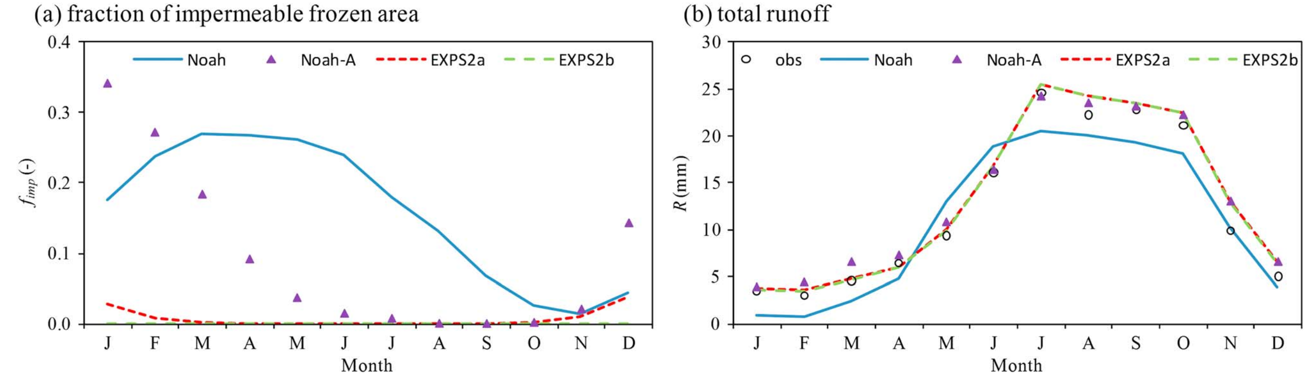

Figure 12. Comparisons of the measured and simulated monthly averaged (a) fraction of impermeable frozen area and (b) total runoff produced by EXPS2a and EXPS2b for the period of July 2002–December 2009.

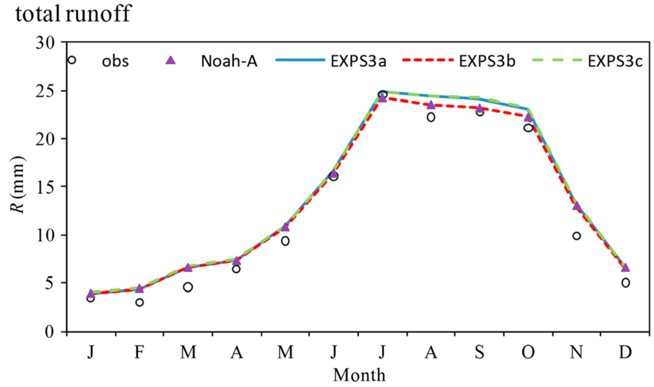

Figure 13. Comparisons of the measured and simulated monthly averaged total runoff produced by EXPS3a–S3c for the period of July 2002–December 2009.

7.2. Impeding Effect of Frozen Ground

Section 6 also demonstrates that the fractional impermeable frozen area, f_{imp}, plays a crucial role in simulating the runoff production for the source region of the Yellow River (SRYR). Noah-A, in which f_{imp} is calculated using the ice content in the top 1 m, performs better than Noah that uses by default the ice content present within the entire 2 m column. Two additional experiments are carried out to investigate the sensitivity of the modeled runoff for the f_{imp} computed with ice contents from different soil depths. One experiment uses the ice content of the top two layers (0.4 m) to calculate f_{imp} (hereafter EXPS2a) and the other one utilizes only the upper layer (0.1 m, hereafter EXPS2b), while all other settings remain as in Noah-A.

Figure 12 shows the monthly and area-averaged f_{imp} and total runoff (R) resulting from EXPS2a and EXPS2b, whereby the measurements as well as the Noah and Noah-A simulations are added as well for comparison purposes. Further, the error statistics computed between the measured and simulated R are included in Table 3. Figure 12a illustrates that the usage of a shallower soil depth for the ice content produces less f_{imp} and approaches zero for EXPS2b. This shows that Noah does not invoke the impeding effect of frozen ground on infiltration, which marginally affects the model performance as indicated by Figure 12b as well as the error statistics listed in Table 3. The explanation for this is that in general the potential R_s source in the SRYR during the cold season is limited by the water availability (e.g., precipitation and snowmelt). Also, *Pitman et al.* [1999] have recommended that LSMs should not include the effect of frozen ground in the runoff formulation for coarse grid simulations as frozen soils remain permeable due to the development of a soil structure with cracks and macropores that facilitate preferential pathways.

7.3. Impact of the Selected Vegetation and Soil Input Data Sets

The global WRF geographic input data set is adopted in this study to characterize the land surface conditions across the SRYR (section 4.2) and is based on the MODIS land use and FAO soil texture map. The logical question is whether these global data sets accurately represent the SRYR land surface conditions and how the associated uncertainty impacts the Noah run simulations. Recent initiatives have been undertaken to improve the characterization of the soil and vegetation conditions across China. For instance, the 1 km spatial resolution Multi-source Integrated Chinese Land Cover (MICLCover; http://westdc.westgis.ac.cn/data/2cc2bf61-06c9-493b-9397-e6c5e0f0bebc, last verified on 21 December 2015) data set has been developed by combining multisource land use maps, which has been shown to provide a more accurate land cover information compared to the global MODIS data set [*Ran et al.*, 2012]. Further, the China Soil Database (http://globalchange.bnu.edu.cn/research/data, last verified on 21 December 2015) was developed by the Land-Atmosphere Interaction Research Group at Beijing Normal University (BNU) and provides soil property information for China with a 1 km spatial resolution based on 8595 soil profiles collected across the country from the Second National Soil Survey and can be used for regional climate and land surface modeling purposes [*Shangguan et al.*, 2012; *Shangguan et al.*, 2013].

With the newly available soil and land cover data sets for China, three additional experiments are carried out to investigate the impact of the selected WRF geographic soil and vegetation data sets on the simulated runoff. One experiment uses the MICLCover land use and the FAO soil texture as input (hereafter EXPS3a), the second adopts the MODIS land use and BNU soil texture (EXPS3b), and the third utilizes the MICLCover land use and BNU soil texture, while all other settings remain as in Noah-A. It should be noted that the BNU soil texture is derived from the available soil particle size distribution [*Shangguan et al.*, 2012].

Further, all the vegetation and soil data sets are interpolated to the coarser 0.1° spatial resolution to match with the ITPCAS atmospheric forcing (section 4.1), where the resulting land use and soil texture maps (Figures B1 and B2) as well as the associate parameterizations are given in Appendix B. Both MICLCover and MODIS land use maps use the International Geosphere-Biosphere Programme (IGBP) land cover classification system, and the BNU soil texture map is produced to share the identical soil classification system as FAO map. It can be deduced from the maps that alpine grasslands and loamy soils dominate the land surface conditions in the SRYR regardless of the data source even though the newly developed MICLCover and BNU maps include additional soil and vegetation types and a larger spatial variability in comparison to the WRF data set.

Figure 13 shows the monthly and area-averaged total runoff (*R*) resulting from EXPS3a–S3c, whereby the error statistics computed between the measured and simulated *R* are included in Table 3. In general, EXPS3a–S3c produce comparable results as Noah-A, where it can be concluded that the impact of the selected vegetation and soil input data sets is inferior to the effect of the model physics in the *R* simulation. This is also expected because of the dominance of alpine grasslands and loamy soils in the both land use and soil texture data sets. Nevertheless, some differences are noted among the *R* results simulated for the months between July and October. A strict validation of vegetation and soil data sets is recommended and may further reduce the uncertainties involving regional climate and land surface modeling but reaches beyond the scope of the presented research.

8. Summary and Conclusions

In this paper, we investigate the impact of various Noah model physics options, validated at the point scale, for their ability to reproduce the runoff at the catchment scale through comparison with monthly discharge measured in the source region of the Yellow River (SRYR) for the period from 2001 to 2010. For application of the Noah model to the SRYR at catchment scale, three sets of augmentations are selected that enhance the descriptions of (i) turbulent and soil heat transport, (ii) soil water flow, and (iii) frozen ground processes. Accordingly, five numerical experiments are designed, namely, a control run with the default model physics (hereafter Noah), three runs each with one of the selected augmentations (hereafter Noah-H, Noah-W, and Noah-F, respectively), and a run whereby all augmentations are implemented (hereafter Noah-A). All Noah model runs adopt their main soil and vegetation parameterizations from the Weather Research and Forecasting (WRF) model geographic input data set and are driven by the ITPCAS atmospheric forcing data set as well as initialized using a single-year recurrent spin-up to achieve the equilibrium model states. In addition, the China Soil Database provides the organic matter content for the updated soil thermal and hydraulic parameterizations.

A point-scale assessment is performed through comparisons of the five simulations with in situ latent heat flux (*LE*), soil moisture (θ), and soil temperature (T_s) profile measurements for the period from November 2009 to December 2010. The results illustrate that the *LE* overestimation and T_s underestimation across the profile using the default Noah model are greatly resolved with the augmentations applied for the Noah-H experimental run. The default θ underestimation is significantly improved by including the parameterization of the vertical soil heterogeneity as in Noah-W. However, improvement in the simulations of *LE*, T_s, and θ_{liq} is only achieved by including all selected augmentations (e.g., Noah-A model run), which leads to reductions in the RMSE of about 15, 28, 43, 64, and 61% for *LE*, T_{s5}, T_{s25}, θ_{liq5}, and θ_{liq25}, respectively.

Monthly streamflow data measured at the outlet of the SRYR from July 2002 to December 2009 are utilized to quantify the model's ability to reproduce the runoff regime at the catchment scale. The default Noah model is able to adequately capture the observed total runoff (*R*) dynamics but underestimates the magnitude of the monthly *R*. Although the largest coefficient of determination (R^2) is obtained with Noah-H, large overestimations are generally found for the summer months due to the excessive release of water from the bottom of the soil column (e.g., base flow, R_b). In contrast, the Noah-W runoff yields the lowest R^2 that can be associated with the wrongly simulated *R* peak caused by the surface runoff (R_s)-dominated *R* due to amplified impeding effect of frozen ground. This effect is strongly reduced using augmentations applied with Noah-F allowing more water to infiltrate and a larger R_b component than Noah-W, which is still insufficient to adequately reproduce the measurements.

The best agreement between the simulated and measured monthly R yields is in the Noah run, whereby all selected augmentations are invoked (Noah-A) with improved error statistics of about 24% and 19% in comparison to the default performance for ME and RMSE, respectively. The combinations of the augmentations selected for Noah-H, Noah-W, and Noah-F properly simulate the liquid moisture content across the soil profile and the permeability of frozen ground. In addition, a warmer soil profile and sufficient infiltration into the soil profile are simulated leading to a R_b-dominated runoff regime, whereby the R_s contribution is still important to achieve a match with the measurements.

Although each of the five experiments produces similar spatial R patterns that generally follow the applied precipitation fields, significant differences are found in the magnitude as well as the partitioning of R into R_s and R_b. For instance, Noah-W provides the largest fractional impermeable frozen ground (f_{imp}), and thus, the R is dominated by the R_s component. On the other hand, Noah-A produces a smaller f_{imp} and allows more water to infiltrate during spring, the rainy summer, and snowmelt season, which enables a year-round release of water from the soil bottom resulting in a superior estimate of the measured hydrograph.

Three additional experiments are conducted to investigate different combinations of the augmentations for their performance at point- and catchment-scale simulations, which further confirms the superiority of Noah-A that all selected augmentations are invoked. Further, a sensitivity experiment illustrates that within the Noah-A structure and for the selected study area, the impeding effect of frozen ground has a marginal impact on model performance. Similar findings were previously reported by *Pitman et al.* [1999], in which they concluded that across large domains, frozen soils remain permeable. Moreover, another sensitivity experiment shows that the impact of different vegetation and soil input data sets is inferior to the effect of Noah model physics in simulating R over the SRYR.

This study demonstrates that thorough understanding of the predominantly vertical heat and water exchange processes at the land-atmosphere interface is needed to correctly simulate the runoff produced in the seasonally frozen and high-altitude SRYR at the catchment scale. In addition, the simulation with the augmented Noah model eloquently illustrates for the study period that the runoff production regime of SRYR is dominated year-round by the R_b component, while the default Noah underestimates its importance during the winter and spring seasons.

The research presented in this manuscript focuses on the runoff production simulated for the SRYR by Noah model. However, additional work is still needed to make reliable streamflow forecasts, where ideally, the effects of lakes, groundwater dynamics, and river routing are also included in the model structure. The improved representation of water cycle processes in the Noah model will allow it to further assist in understanding hydrology across the Asian water towers that is of paramount importance for developing reliable streamflow projections under a changing climate of this region.

Appendix A: Noah Model Physics

A1. Soil Heat Flow

The transport of heat through the soil column is governed by the thermal diffusion equation with a source/sink term to account for soil moisture phase transitions [*Koren et al.*, 1999]:

$$C_s(\theta, \theta_{\text{ice}})\frac{\partial T}{\partial t} = \frac{\partial}{\partial z}\left(\kappa_h(\theta, \theta_{\text{ice}})\frac{\partial T}{\partial z}\right) + \rho_{\text{ice}} L_f \frac{\partial \theta_{\text{ice}}}{\partial t} \tag{A1}$$

where T is the soil temperature (K), t is the time (s), z is the soil depth (m), ρ_{ice} is the density of ice (kg m^{-3}), L_f is the latent heat of fusion (J kg^{-1}), θ is the total soil water content (m^3 m^{-3}), θ_{ice} is the soil ice content (m^3 m^{-3}), κ_h is the thermal heat conductivity (W m^{-1} K^{-1}), and C_s is the thermal heat capacity (J m^{-3} K^{-1}). Both κ_h and C_s depend on all constituents of the soil matrix (e.g., θ and θ_{ice}), and the details of the soil thermal parameterization can be found in *Peters-Lidard et al.* [1998]. The heat source/sink term is determined by the soil water phase equilibrium estimated using the water potential freezing point depression equation as well as the available heat [*Koren et al.*, 1999].

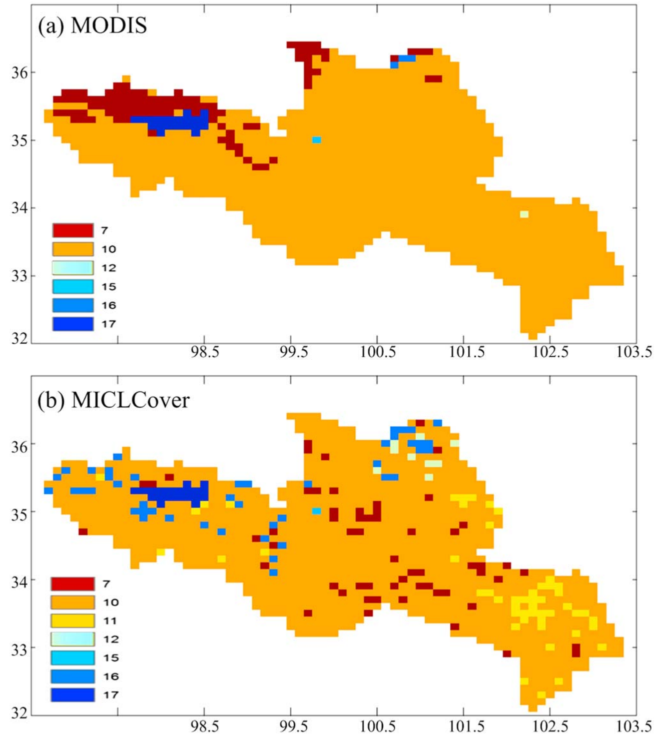

Figure B1. Vegetation-type maps according to the IGBP classification system for the SRYR derived from (a) MODIS and (b) MICLCover data sets: 7–open shrublands, 10–grasslands, 11–permanent wetlands, 12–croplands, 15–snow and ice, 16–barren or sparsely vegetated, and 17–water.

A2. Soil Water Flow

The diffusivity form of Richards' equation is utilized to estimate unfrozen or liquid soil water movement with the assumption that liquid water flow in the frozen soil is analogous to that in unfrozen soil [*Koren et al.*, 1999]:

$$\frac{\partial\theta_{\text{liq}}}{\partial t}=\frac{\partial}{\partial z}\left(D\left(\theta_{\text{liq}},\theta_{\text{ice}}\right)\frac{\partial\theta_{\text{liq}}}{\partial z}\right)+\frac{\partial K\left(\theta_{\text{liq}}\right)}{\partial z}+S(\theta) \tag{A2}$$

where θ_{liq} is the unfrozen/liquid soil water content (m^3 m^{-3}), D is the soil water diffusivity (m^2 s^{-1}), K is the hydraulic conductivity (m s^{-1}), and S represents the sources and sinks (i.e., infiltration and evapotranspiration, m s^{-1}).

The empirical soil hydraulic scheme proposed by *Campbell* [1974] is modified to parameterize the K-θ and D-θ relationships for the frozen ground condition as a function of soil texture [*Cosby et al.*, 1984]:

$$K\left(\theta_{\text{liq}}\right)=K_s\left(\theta_{\text{liq}}/\theta_s\right)^{2b+3} \tag{A3}$$

$$D\left(\theta_{\text{liq}},\theta_{\text{ice}}\right)=f_{\text{un}}\cdot D_s\left(\theta_{\text{liq}}/\theta_s\right)^{b+2}+\left(1-f_{\text{un}}\right)\cdot D_s\left(\min\left(\theta_{\text{liq}},0.05\right)/\theta_s\right)^{b+2} \tag{A4}$$

$$f_{\text{un}}=1/\left[1+\left(500\cdot\max\left(\sum_{i=1}^{4}\theta_{\text{ice},i}\right)\right)^3\right] \tag{A5}$$

where K_s is the saturated hydraulic conductivity (m s^{-1}), θ_s is the porosity (m^3 m^{-3}), b is an empirical parameter (−) related to the pore size distribution of the soil matrix, D_s is the saturated soil water diffusivity (m^2 s^{-1}), and f_{un} is an empirical factor to avoid the numerical truncation error that affects the estimation of unfrozen water movement.

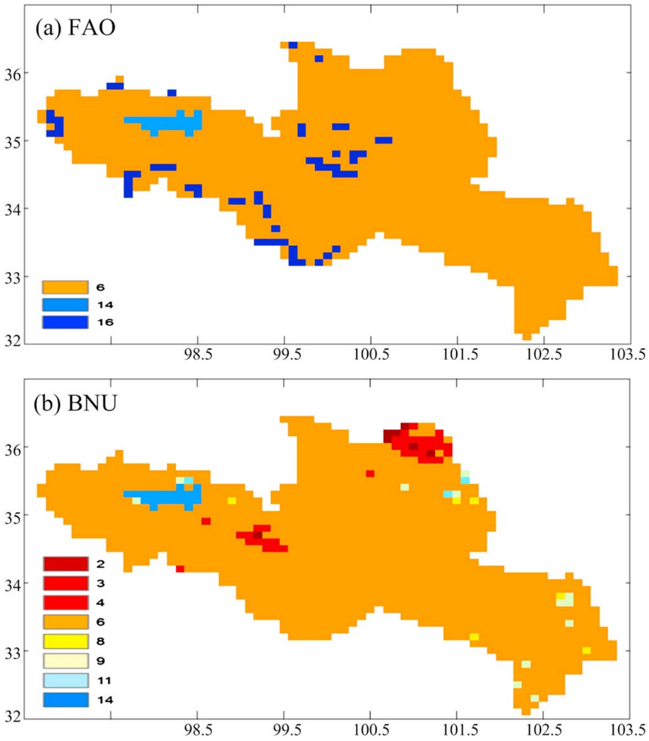

Figure B2. Soil-type maps following the FAO soil classification system for the SRYR derived from (a) FAO and (b) BNU data sets: 2–loamy sand, 3–sandy loam, 4–silt loam, 6–loam, 8–silty clay loam, 9–clay loam, 11–silty clay, 14–water, and 16–other (land ice).

A3. Surface Runoff and Drainage

The surface runoff (R_s, in m s^{-1}) includes the direct runoff from the impermeable frozen area (f_{imp}, −) and the infiltration-excess runoff from the rest of the model grid [*Koren et al.*, 1999; *Schaake et al.*, 1996]:

$$R_s = \left\{ f_{\mathrm{imp}} P_x + \left(1 - f_{\mathrm{imp}}\right) \frac{P_x^2}{P_x + W_d[1 - \exp(-K_{\mathrm{dt}}\Delta t)]} \right\} / \Delta t \tag{A6}$$

where P_x is the precipitation reaching the ground (m), W_d is the total soil moisture deficit in the soil column (m), K_{dt} is an empirical constant and taken as 3.0 d^{-1}, Δt is the model time step (s), and the fraction of impermeable frozen area is approximated by a gamma distribution of soil ice content (W_{ice}, m):

$$f_{\mathrm{imp}} = e^{-v} \sum_{i=1}^{\alpha} \frac{v^{\alpha - i}}{\Gamma(\alpha - i + 1)} \tag{A7}$$

$$v = \alpha \frac{W_{\mathrm{cr}}}{W_{\mathrm{ice}}} \tag{A8}$$

Table B1. Soil Hydraulic and Thermal Parameters Predefined in Noah LSM

Texture	θ_s (m^3 m^{-3})	K_s (10^{-6} m s^{-1})	ψ_s (m)	b (−)	qtz (−)[a]
Loamy sand	0.421	14.1	−0.036	4.26	0.82
Sandy loam	0.434	5.23	−0.141	4.74	0.60
Silt loam	0.476	2.81	−0.759	5.33	0.25
Loam	0.439	3.38	−0.355	5.25	0.40
Silty clay loam	0.464	2.04	−0.617	8.72	0.10
Clay loam	0.465	2.45	−0.263	8.17	0.35
Silty clay	0.468	1.34	−0.324	10.39	0.10
Other (land ice)	0.421	5.14	−0.036	4.26	0.25
Organic matter	0.830	0.10	−0.0101	12.00	-

[a] *qtz* is the volumetric quartz fraction.

$$W_{\mathrm{ice}} = \sum_{i=1}^{4} \theta_{\mathrm{ice},i} \cdot \Delta z_i \qquad \text{(A9)}$$

where Δz is the depth of each soil layer (m), α is a shape parameter of the gamma distribution and taken as 3 (−), and W_{cr} is the critical ice content above which the frozen ground is impermeable and is taken as 0.15 m.

Table B2. Vegetation Parameters Predefined in Noah LSM

Land Cover	*nroot* (−)[a]	$z_{0\mathrm{mmin}}$ (m)[a]	$z_{0\mathrm{mmax}}$ (m)[a]
Open shrublands	3	0.01	0.05
Grasslands	3	0.011	0.035
Permanent wetlands	2	0.30	0.30
Croplands	3	0.05	0.15
Barren	1	0.011	0.011

[a] *nroot* is the total number of root layers, and $z_{0\mathrm{mmin}}$ and $z_{0\mathrm{mmax}}$ are the maximum and minimum values of $z_{0\mathrm{m}}$.

Gravitational free drainage (R_b, in m s^{-1}) from the model bottom is formulated as

$$R_b = \mathrm{slope} \cdot K\left(\theta_{\mathrm{liq},4}\right) \qquad \text{(A10)}$$

where *slope* is a slope index between 0 and 1 that is depending on the grid slope derived from the digital elevation model and K ($\theta_{\mathrm{liq},4}$) is the hydraulic conductivity of the bottom soil layer (m s^{-1}) that can be estimated by equation (A3).

Appendix B: Vegetation and Soil Data Sets

B1. Vegetation and Soil Maps

The land cover maps derived from MODIS and MICLCover data sets for the source region of the Yellow River (SRYR) are shown in Figure B1, and the soil texture maps derived from FAO and BNU soil databases are shown in Figure B2. Detailed descriptions of these data sets are given in sections 4.2 and 7.3.

B2. Vegetation and Soil Parameters

Soil and vegetation parameters are specified for each vegetation and soil types by means of Noah's default look-up tables with the exception of momentum roughness lengths ($z_{0\mathrm{m}}$) for grassland and bare ground, which are set to 0.035 and 0.011 m, respectively, following *Zheng et al.* [2014]. Moreover, the sapric peat parameterization reported by *Letts et al.* [2000] is adopted to represent the hydraulic properties for pure organic matter. The soil and vegetation parameter sets specified for this study are given in Tables B1 and B2, respectively. Additionally, the heat capacities of mineral and organic matter are taken, respectively, as 2.0×10^6 and 2.5×10^6 J m^{-3} K^{-1}, while the heat conductivity of organic matter is taken as 0.25 W m^{-1} K^{-1} according to *Lawrence and Slater* [2008].

Acknowledgments
This study was supported by funding from the FP7 CEOP-AEGIS project funded by the European Commission through the FP7 program, the Chinese Academy of Sciences Fellowship for Young International Scientists (grant 2012Y1ZA0013), the Key Research Program of the Chinese Academy of Sciences (grant KZZD-EW-13), and the National Natural Science Foundation of China (grants 41405079 and 41130961). The forcing data set used in this study was developed by Data Assimilation and Modeling Center for Tibetan Multi-spheres in ITP/CAS. The China Soil Database was developed by Land-Atmosphere Interaction Research Group at Beijing Normal University. The Multi-source Integrated Chinese Land Cover was obtained from WestDC data center. The global WRF geographic input data set was obtained from WRF Users' Page. The measurements used in this study were provided by Zoige Plateau Wetland Ecosystem Research Station of CAREERI/CAS. For data access, please contact Jun Wen (jwen@lzb.ac.cn) and Yu Zhang (yuzhang@lzb.ac.cn).

References

Ahuja, L. R., J. W. Naney, R. E. Green, and D. R. Nielsen (1984), Macroporosity to characterize spatial variability of hydraulic conductivity and effects of land management, *Soil Sci. Soc. Am. J.*, *48*(4), 699–702.

Balsamo, G., A. Beljaars, K. Scipal, P. Viterbo, B. van den Hurk, M. Hirschi, and A. K. Betts (2009), A revised hydrology for the ECMWF model: Verification from field site to terrestrial water storage and impact in the integrated forecast system, *J. Hydrometeorol.*, *10*(3), 623–643.

Beven, K. (1982), On subsurface stormflow: An analysis of response times, *Hydrol. Sci. J.*, *27*(4), 505–521.

Cai, X., Z.-L. Yang, C. H. David, G.-Y. Niu, and M. Rodell (2014), Hydrological evaluation of the Noah-MP land surface model for the Mississippi river basin, *J. Geophys. Res. Atmos.*, *119*, 23–38, doi:10.1002/2013JD020792.

Campbell, G. S. (1974), A simple method for determining unsaturated conductivity from moisture retention data, *Soil Sci.*, *117*(6), 311–314.

Chen, F., and Y. Zhang (2009), On the coupling strength between the land surface and the atmosphere: From viewpoint of surface exchange coefficients, *Geophys. Res. Lett.*, *36*, L10404, doi:10.1029/2009GL037980.

Chen, F., K. Mitchell, J. Schaake, Y. Xue, H.-L. Pan, V. Koren, Q. Y. Duan, M. Ek, and A. Betts (1996), Modeling of land surface evaporation by four schemes and comparison with FIFE observations, *J. Geophys. Res.*, *101*(D3), 7251–7268, doi:10.1029/95JD02165.

Chen, F., et al. (2007), Description and evaluation of the characteristics of the NCAR High-Resolution Land Data Assimilation System, *J. Appl. Meteorol. Climatol.*, *46*(6), 694–713.

Chen, Y., K. Yang, J. He, J. Qin, J. Shi, J. Du, and Q. He (2011), Improving land surface temperature modeling for dry land of China, *J. Geophys. Res.*, *116*, D20104, doi:10.1029/2011JD015921.

Chen, Y., K. Yang, J. Qin, L. Zhao, W. Tang, and M. Han (2013), Evaluation of AMSR-E retrievals and GLDAS simulations against observations of a soil moisture network on the central Tibetan Plateau, *J. Geophys. Res. Atmos.*, *118*, 4466–4475, doi:10.1002/jgrd.50301.

Cheng, G., and T. Wu (2007), Responses of permafrost to climate change and their environmental significance, Qinghai-Tibet Plateau, *J. Geophys. Res.*, *112*, F02S03, doi:10.1029/2006JF000631.

Cherkauer, K. A., and D. P. Lettenmaier (1999), Hydrologic effects of frozen soils in the upper Mississippi River basin, *J. Geophys. Res.*, *104*(D16), 19,599–19,610, doi:10.1029/1999JD900337.

Cosby, B. J., G. M. Hornberger, R. B. Clapp, and T. R. Ginn (1984), A statistical exploration of the relationships of soil moisture characteristics to the physical properties of soils, *Water Resour. Res.*, *20*(6), 682–690, doi:10.1029/WR020i006p00682.

Cuo, L., Y. Zhang, Y. Gao, Z. Hao, and L. Cairang (2013), The impacts of climate change and land cover/use transition on the hydrology in the upper Yellow River Basin, China, *J. Hydrol.*, *502*, 37–52, doi:10.1029/WR020i006p00682.

Dankers, R., E. J. Burke, and J. Price (2011), Simulation of permafrost and seasonal thaw depth in the JULES land surface scheme, *Cryosphere*, *5*(3), 773–790.

de Vries, D. A. (1963), Thermal properties of soils, in *Physics of Plant Environment*, edited by W. R. van Wijk, pp. 210–235, North-Holland, Amsterdam.

Dente, L., Z. Vekerdy, J. Wen, and Z. Su (2012), Maqu network for validation of satellite-derived soil moisture products, *Int. J. Appl. Earth Observ. Geoinfo.*, *17*, 55–65.

Ek, M. B., K. E. Mitchell, Y. Lin, E. Rogers, P. Grunmann, V. Koren, G. Gayno, and J. D. Tarpley (2003), Implementation of Noah land surface model advances in the National Centers for Environmental Prediction operational mesoscale Eta model, *J. Geophys. Res.*, *108*(D22), 8851, doi:10.1029/2002JD003296.

Farouki, O. T. (1986), *Thermal Properties of Soils*, 136 pp., Trans Tech, Clausthal-Zellerfeld, Gemany.

Finney, D. L., E. Blyth, and R. Ellis (2012), Improved modelling of Siberian river flow through the use of an alternative frozen soil hydrology scheme in a land surface model, *Cryosphere*, *6*(4), 859–870.

Gao, H., X. He, B. Ye, and J. Pu (2012), Modeling the runoff and glacier mass balance in a small watershed on the central Tibetan Plateau, China, from 1955 to 2008, *Hydrol. Processes*, *26*(11), 1593–1603.

Gouttevin, I., G. Krinner, P. Ciais, J. Polcher, and C. Legout (2012), Multi-scale validation of a new soil freezing scheme for a land-surface model with physically-based hydrology, *Cryosphere*, *6*(2), 407–430.

Guo, D., and H. Wang (2013), Simulation of permafrost and seasonally frozen ground conditions on the Tibetan Plateau, 1981–2010, *J. Geophys. Res. Atmos.*, *118*, 5216–5230, doi:10.1002/jgrd.50457.

Hills, R. G., I. Porro, D. B. Hudson, and P. J. Wierenga (1989), Modeling one-dimensional infiltration into very dry soils: 1. Model development and evaluation, *Water Resour. Res.*, *25*(6), 1259–1269, doi:10.1029/WR025i006p01259.

Hu, Y., S. Maskey, S. Uhlenbrook, and H. Zhao (2011), Streamflow trends and climate linkages in the source region of the Yellow River, China, *Hydrol. Processes*, *25*(22), 3399–3411.

Huffman, G. J., D. T. Bolvin, E. J. Nelkin, D. B. Wolff, R. F. Adler, G. Gu, Y. Hong, K. P. Bowman, and E. F. Stocker (2007), The TRMM Multisatellite Precipitation Analysis (TMPA): Quasi-global, multiyear, combined-sensor precipitation estimates at fine scales, *J. Hydrometeorol.*, *8*(1), 38–55.

Immerzeel, W. W., L. P. H. van Beek, and M. F. P. Bierkens (2010), Climate change will affect the Asian water towers, *Science*, *328*(5984), 1382–1385.

Jackson, R. B., J. Canadell, J. R. Ehleringer, H. A. Mooney, O. E. Sala, and E. D. Schulze (1996), A global analysis of root distributions for terrestrial biomes, *Oecologia*, *108*(3), 389–411.

Jin, H., R. He, G. Cheng, Q. Wu, S. Wang, L. Lü, and X. Chang (2009), Changes in frozen ground in the source area of the Yellow River on the Qinghai–Tibet Plateau, China, and their eco-environmental impacts, *Environ. Res. Lett.*, *4*(4), 045206.

Johansen, O. (1975), Thermal conductivity of soils, PhD thesis, 236 pp., Univ. of Trondheim.

Koike, T. (2004), The coordinated enhanced observing period—An initial step for integrated global water cycle observation, *WMO Bull.*, *53*(2), 115–121.

Koike, T., T. Yasunari, J. Wang, and T. Yao (1999), GAME-Tibet IOP summary report, *Proceedings of the 1st International Workshop on GAME-Tibet*, 1-2.

Koren, V., J. Schaake, K. Mitchell, Q. Y. Duan, F. Chen, and J. M. Baker (1999), A parameterization of snowpack and frozen ground intended for NCEP weather and climate models, *J. Geophys. Res.*, *104*(D16), 19,569–19,585, doi:10.1029/1999JD900232.

Lawrence, D. M., and A. G. Slater (2008), Incorporating organic soil into a global climate model, *Clim. Dyn.*, *30*(2–3), 145–160.

Letts, M. G., N. T. Roulet, N. T. Comer, M. R. Skarupa, and D. L. Verseghy (2000), Parametrization of peatland hydraulic properties for the Canadian land surface scheme, *Atmos. Ocean*, *38*(1), 141–160.

Li, Q., S. Sun, and Y. Xue (2010), Analyses and development of a hierarchy of frozen soil models for cold region study, *J. Geophys. Res.*, *115*, D03107, doi:10.1029/2009JD012530.

Lim, Y.-J., J. Hong, and T.-Y. Lee (2012), Spin-up behavior of soil moisture content over East Asia in a land surface model, *Meteorol. Atmos. Phys.*, *118*(3–4), 151–161.

Livneh, B., P. J. Restrepo, and D. P. Lettenmaier (2011), Development of a unified land model for prediction of surface hydrology and land–atmosphere interactions, *J. Hydrometeorol.*, *12*(6), 1299–1320.

Luo, L., et al. (2003), Effects of frozen soil on soil temperature, spring infiltration, and runoff: Results from the PILPS 2(d) experiment at Valdai, Russia, *J. Hydrometeorol.*, *4*(2), 334–351.

Lutz, A. F., W. W. Immerzeel, A. B. Shrestha, and M. F. P. Bierkens (2014), Consistent increase in High Asia's runoff due to increasing glacier melt and precipitation, *Nat. Clim. Change*, *4*(7), 587–592.

Ma, Y., S. Kang, L. Zhu, B. Xu, L. Tian, and T. Yao (2008), Roof of the World: Tibetan observation and research platform, *Bull. Am. Meteorol. Soc.*, *89*(10), 1487–1492.

Mahrt, L., and M. Ek (1984), The influence of atmospheric stability on potential evaporation, *J. Climate Appl. Meteorol.*, *23*(2), 222–234.

Mahrt, L., and H. Pan (1984), A two-layer model of soil hydrology, *Boundary Layer Meteorol.*, *29*(1), 1–20.

Mitchell, K. E., et al. (2004), The multi-institution North American Land Data Assimilation System (NLDAS): Utilizing multiple GCIP products and partners in a continental distributed hydrological modeling system, *J. Geophys. Res.*, *109*, D07S90, doi:10.1029/2003JD003823.

Niu, G.-Y., and Z.-L. Yang (2006), Effects of frozen soil on snowmelt runoff and soil water storage at a continental scale, *J. Hydrometeorol.*, *7*(5), 937–952.

Niu, G.-Y., et al. (2011), The community Noah land surface model with multiparameterization options (Noah-MP): 1. Model description and evaluation with local-scale measurements, *J. Geophys. Res.*, *116*, D12109, doi:10.1029/2010JD015139.

Pan, H. L., and L. Mahrt (1987), Interaction between soil hydrology and boundary-layer development, *Boundary Layer Meteorol.*, *38*(1–2), 185–202.

Peters-Lidard, C. D., E. Blackburn, X. Liang, and E. F. Wood (1998), The effect of soil thermal conductivity parameterization on surface energy fluxes and temperatures, *J. Atmos. Sci.*, *55*(7), 1209–1224.

Pitman, A. J., A. G. Slater, C. E. Desborough, and M. Zhao (1999), Uncertainty in the simulation of runoff due to the parameterization of frozen soil moisture using the Global Soil Wetness Project methodology, *J. Geophys. Res.*, *104*(D14), 16,879–16,888, doi:10.1029/1999JD900261.

Ran, Y. H., X. Li, L. Lu, and Z. Y. Li (2012), Large-scale land cover mapping with the integration of multi-source information based on the Dempster–Shafer theory, *Int. J. Geogr. Inf. Sci.*, *26*(1), 169–191.

Rodell, M., et al. (2004), The Global Land Data Assimilation System, *Bull. Am. Meteorol. Soc.*, *85*(3), 381–394.

Rosero, E., Z.-L. Yang, T. Wagener, L. E. Gulden, S. Yatheendradas, and G.-Y. Niu (2010), Quantifying parameter sensitivity, interaction, and transferability in hydrologically enhanced versions of the Noah land surface model over transition zones during the warm season, *J. Geophys. Res.*, *115*, D03106, doi:10.1029/2009JD012035.

Salama, M. S., R. Van der Velde, L. Zhong, Y. Ma, M. Ofwono, and Z. Su (2012), Decadal variations of land surface temperature anomalies observed over the Tibetan Plateau by the Special Sensor Microwave Imager (SSM/I) from 1987 to 2008, *Clim. Change*, *114*(3–4), 769–781.

Sato, Y., X. Ma, J. Xu, M. Matsuoka, H. Zheng, C. Liu, and Y. Fukushima (2008), Analysis of long-term water balance in the source area of the Yellow River basin, *Hydrol. Processes*, *22*(11), 1618–1629.

Saxton, K. E., and W. J. Rawls (2006), Soil water characteristic estimates by texture and organic matter for hydrologic solutions, *Soil Sci. Soc. Am. J.*, *70*(5), 1569–1578.

Schaake, J. C., V. I. Koren, Q.-Y. Duan, K. Mitchell, and F. Chen (1996), Simple water balance model for estimating runoff at different spatial and temporal scales, *J. Geophys. Res.*, *101*(D3), 7461–7475, doi:10.1029/95JD02892.

Shangguan, W., Y. Dai, B. Liu, A. Ye, and H. Yuan (2012), A soil particle-size distribution dataset for regional land and climate modelling in China, *Geoderma*, *171–172*, 85–91.

Shangguan, W., et al. (2013), A China data set of soil properties for land surface modeling, *J. Adv. Model. Earth Syst.*, *5*(2), 212–224.

Shrestha, R., and P. Houser (2010), A heterogeneous land surface model initialization study, *J. Geophys. Res.*, *115*, D19111, doi:10.1029/2009JD013252.

Slater, A. G., T. J. Bohn, J. L. McCreight, M. C. Serreze, and D. P. Lettenmaier (2007), A multimodel simulation of pan-Arctic hydrology, *J. Geophys. Res.*, *112*, G04S45, doi:10.1029/2006JG000303.

Su, Z., J. Wen, L. Dente, R. van der Velde, L. Wang, Y. Ma, K. Yang, and Z. Hu (2011), The Tibetan Plateau observatory of plateau scale soil moisture and soil temperature (Tibet-Obs) for quantifying uncertainties in coarse resolution satellite and model products, *Hydrol. Earth Syst. Sci.*, *15*(7), 2303–2316.

Su, Z., P. de Rosnay, J. Wen, L. Wang, and Y. Zeng (2013), Evaluation of ECMWF's soil moisture analyses using observations on the Tibetan Plateau, *J. Geophys. Res. Atmos.*, *118*, 5304–5318, doi:10.1002/jgrd.50468.

van der Velde, R., Z. Su, M. Ek, M. Rodell, and Y. Ma (2009), Influence of thermodynamic soil and vegetation parameterizations on the simulation of soil temperature states and surface fluxes by the Noah LSM over a Tibetan Plateau site, *Hydrol. Earth Syst. Sci.*, *13*(6), 759–777.

Viterbo, P., A. Beljaars, J.-F. Mahfouf, and J. Teixeira (1999), The representation of soil moisture freezing and its impact on the stable boundary layer, *Q. J. R. Meteorol. Soc.*, *125*(559), 2401–2426.

Wang, G., H. Hu, and T. Li (2009), The influence of freeze–thaw cycles of active soil layer on surface runoff in a permafrost watershed, *J. Hydrol.*, *375*(3–4), 438–449.

Wang, G., G. Liu, and C. Li (2012), Effects of changes in alpine grassland vegetation cover on hillslope hydrological processes in a permafrost watershed, *J. Hydrol.*, *444–445*, 22–33.

Wu, Q., and T. Zhang (2010), Changes in active layer thickness over the Qinghai-Tibetan Plateau from 1995 to 2007, *J. Geophys. Res.*, *115*, D09107, doi:10.1029/2009JD012974.

Wu, T., L. Zhao, R. Li, Q. Wang, C. Xie, and Q. Pang (2013), Recent ground surface warming and its effects on permafrost on the central Qinghai-Tibet Plateau, *Int. J. Climatol.*, *33*(4), 920–930.

Xia, Y., et al. (2012), Continental-scale water and energy flux analysis and validation for the North American Land Data Assimilation System project phase 2 (NLDAS-2): 1. Intercomparison and application of model products, *J. Geophys. Res.*, *117*, D03109, doi:10.1029/2011JD016048.

Xia, Y., J. Sheffield, M. B. Ek, J. Dong, N. Chaney, H. Wei, J. Meng, and E. F. Wood (2014), Evaluation of multi-model simulated soil moisture in NLDAS-2, *J. Hydrol.*, *512*, 107–125.

Xue, B.-L., et al. (2013), Modeling the land surface water and energy cycles of a mesoscale watershed in the central Tibetan Plateau during summer with a distributed hydrological model, *J. Geophys. Res. Atmos.*, *118*, 8857–8868, doi:10.1002/jgrd.50696.

Yang, K., T. Koike, B. Ye, and L. Bastidas (2005), Inverse analysis of the role of soil vertical heterogeneity in controlling surface soil state and energy partition, *J. Geophys. Res.*, *110*, D08101, doi:10.1029/2004JD005500.

Yang, K., Y. Y. Chen, and J. Qin (2009), Some practical notes on the land surface modeling in the Tibetan Plateau, *Hydrol. Earth Syst. Sci.*, *13*(5), 687–701.

Yang, K., J. He, W. Tang, J. Qin, and C. C. K. Cheng (2010), On downward shortwave and longwave radiations over high altitude regions: Observation and modeling in the Tibetan Plateau, *Agr. Forest Meteorol.*, *150*(1), 38–46.

Yang, K., et al. (2013), A multiscale soil moisture and freeze-thaw monitoring network on the third pole, *Bull. Am. Meteorol. Soc.*, *94*(12), 1907–1916.

Yang, Y., J. Fang, C. Ji, and W. Han (2009), Above- and belowground biomass allocation in Tibetan grasslands, *J. Veg. Sci.*, *20*(1), 177–184.

Zeiliguer, A. M., Y. A. Pachepsky, and W. J. Rawls (2000), Estimating water retention of sandy soils using the additivity hypothesis, *Soil Sci.*, *165*(5), 373–383.

Zeng, X., Z. Wang, and A. Wang (2012), Surface skin temperature and the interplay between sensible and ground heat fluxes over arid regions, *J. Hydrometeorol.*, *13*(4), 1359–1370.

Zhang, L., F. Su, D. Yang, Z. Hao, and K. Tong (2013), Discharge regime and simulation for the upstream of major rivers over Tibetan Plateau, *J. Geophys. Res. Atmos.*, *118*, 8500–8518, doi:10.1002/jgrd.50665.

Zhang, Y., S. K. Carey, and W. L. Quinton (2008), Evaluation of the algorithms and parameterizations for ground thawing and freezing simulation in permafrost regions, *J. Geophys. Res.*, *113*, D17116, doi:10.1029/2007JD009343.

Zhang, Y., S. K. Carey, W. L. Quinton, J. R. Janowicz, J. W. Pomeroy, and G. N. Flerchinger (2010), Comparison of algorithms and parameterisations for infiltration into organic-covered permafrost soils, *Hydrol. Earth Syst. Sci.*, *14*(5), 729–750.

Zhang, Y., G. Cheng, X. Li, X. Han, L. Wang, H. Li, X. Chang, and G. N. Flerchinger (2013), Coupling of a simultaneous heat and water model with a distributed hydrological model and evaluation of the combined model in a cold region watershed, *Hydrol. Processes*, *27*(25), 3762–3776.

Zheng, D., R. van der Velde, Z. Su, M. J. Booij, A. Y. Hoekstra, and J. Wen (2014), Assessment of roughness length schemes implemented within the Noah land surface model for high-altitude regions, *J. Hydrometeorol.*, *15*(3), 921–937.

Zheng, D., R. Van der Velde, Z. Su, X. Wang, J. Wen, M. J. Booij, A. Y. Hoekstra, and Y. Chen (2015a), Augmentations to the Noah model physics for application to the Yellow River source area. Part I: Soil water flow, *J. Hydrometeorol.*, *16*(6), 2659–2676.

Zheng, D., R. Van der Velde, Z. Su, X. Wang, J. Wen, M. J. Booij, A. Y. Hoekstra, and Y. Chen (2015b), Augmentations to the Noah model physics for application to the Yellow River source area. Part II: Turbulent heat fluxes and soil heat transport, *J. Hydrometeorol.*, *16*(6), 2677–2694.

Zheng, H., L. Zhang, C. Liu, Q. Shao, and Y. Fukushima (2007), Changes in stream flow regime in headwater catchments of the Yellow River basin since the 1950s, *Hydrol. Processes*, *21*(7), 886–893.

Zhou, D., and R. Huang (2012), Response of water budget to recent climatic changes in the source region of the Yellow River, *Chin. Sci. Bull.*, *57*(17), 2155–2162.